Creep of CarbFix Basalt: Influence of Rock-fluid Interaction

Tiange Xing[1], Hamed O. Ghaffari[1], Ulrich Mok[1], Matej Pec[1]

[1]Department of Earth, Atmospheric and Planetary Sciences, Massachusetts Institute of Technology

Correspondence to: Tiange Xing (tiange@mit.edu)

Abstract. Geological carbon sequestration provides permanent CO_2 storage to mitigate the current high concentration of CO_2 in the atmosphere. CO_2 mineralization in basalts has been proven to be one of the most secure storage options. For successful implementation and future improvements of this technology, the time-dependent deformation behavior of reservoir rocks in presence of reactive fluids needs to be studied in detail. We conducted load stepping creep experiments on basalts from the CarbFix site (Iceland) under several pore fluid conditions (dry, H_2O-saturated and H_2O+CO_2-saturated) at temperature, T≈80°C and effective pressure, P_{eff} = 50 MPa, during which we collected mechanical, acoustic and pore fluid chemistry data. We observed transient creep at stresses as low as 11% of the ultimate failure strength, well below the stress level at the onset of bulk dilatancy. Acoustic emissions (AEs) correlated strongly with strain accumulation, indicating that the creep deformation was a brittle process in agreement with microstructural observations. The rate and magnitude of AEs were higher in fluid-saturated experiments than in dry conditions. We infer that the predominant mechanism governing creep deformation is time- and stress-dependent sub-critical dilatant cracking. Our results suggest that the presence of aqueous fluids exerts first order control on creep deformation of basaltic rocks, while the composition of the fluids plays only a secondary role under the studied conditions.
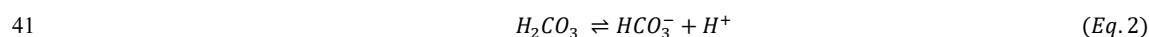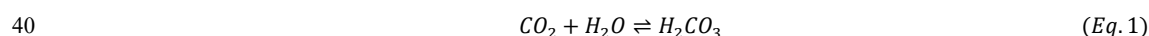
1 Introduction

The concentration of atmospheric CO_2 has seen a significant increase over the last century, raising concerns about the more frequent occurrence of extreme weather, sea-level rise and the projected increase of average global temperature (Broecker, 1975). It is estimated that about 800 Gt CO_2 will need to be stored by the end of the century to keep the global temperature increase below 1.5 ˚C compared to pre-industrial levels (National Academies of Sciences, Engineering, 2019). Such large volumes can practically be stored in the sub-surface. Geological carbon sequestration (GCS) by in-situ carbon mineralization is recognized as one of the most secure, long-term storage solutions (Gislason and Oelkers, 2014; Kelemen and Matter, 2008; Lackner et al., 1995; Mani et al., 2008; Seifritz, 1990; Snæbjörnsdóttir et al., 2020). To date, several pilot projects have been launched to study GCS in basalt reservoirs, including the CarbFix program in Iceland (Callow et al., 2018; Gislason et al., 2010; Oelkers et al., 2008; Snæbjörnsdóttir et al., 2018) and the Wallula basalt (part of Columbia River Basalt Group) sequestration project in Washington, US (McGrail et al., 2006, 2011, 2017; Zakharova et al., 2012).

GCS involves the injection of fluids, either supercritical CO_2 or CO_2 in an aqueous solution, into the formations. Basalts are composed of mafic minerals such as pyroxene ($(Mg,Fe)_2Si_2O_6$), plagioclase ($(Ca,Na)Al_{1.70}Si_{2.30}O_8$), and olivine ($(Mg,Fe)_2SiO_4$) as well as mafic glass, which react with CO_2 to form carbonate minerals (e.g $MgCO_3$, $CaCO_3$,
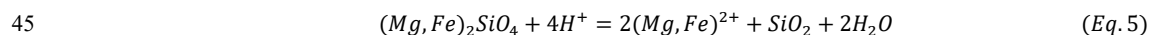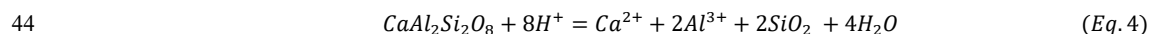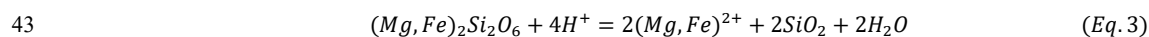
34   FeCO$_3$ etc.), thus binding the injected CO$_2$ in mineral structure (Gislason and Hans, 1987; Hangx and Spiers, 2009;

35   Matter et al., 2007; Oelkers et al., 2008). Carbonation reactions appear to be rapid in natural conditions; more than

36   95% of the CO$_2$ injected into the CarbFix site in Iceland was converted to carbonate minerals in less than 2 years

37   (Matter et al., 2016). Relevant fluid and mineral reactions can be formulated as follows (Hangx and Spiers, 2009;

38   Hansen et al., 2005; Kelemen and Matter, 2008; Oelkers et al., 2008):

39   Dissociation:

$$CO_2 + H_2O \rightleftharpoons H_2CO_3 \qquad\qquad (Eq.\,1)$$

$$H_2CO_3 \rightleftharpoons HCO_3^- + H^+ \qquad\qquad (Eq.\,2)$$

42   Dissolution:

$$(Mg,Fe)_2Si_2O_6 + 4H^+ = 2(Mg,Fe)^{2+} + 2SiO_2 + 2H_2O \qquad\qquad (Eq.\,3)$$

$$CaAl_2Si_2O_8 + 8H^+ = Ca^{2+} + 2Al^{3+} + 2SiO_2 + 4H_2O \qquad\qquad (Eq.\,4)$$

$$(Mg,Fe)_2SiO_4 + 4H^+ = 2(Mg,Fe)^{2+} + SiO_2 + 2H_2O \qquad\qquad (Eq.\,5)$$

46   Precipitation:

$$(Mg,Ca,Fe)^{2+} + HCO_3^- = (Mg,Ca,Fe)CO_3 + H^+ \qquad\qquad (Eq.\,6)$$

48   CO$_2$ is dissolved in water to form an acidic solution (Eq. 1-2). The rocks dissolve to liberate divalent cations (Eq. 3-

49   5), which upon saturation in the fluid, precipitate as carbonate minerals (Eq. 6) further downstream from the injection

50   site.

51   The mechanical and transport behavior of rocks can be significantly affected during GCS by the interaction between

52   rock and fluid, both from a mechanical as well as chemical perspective (Baud et al., 2000; Dunning & Miller, 1985;

53   Heard, 1960; Helmons et al., 2016; Rutter & Hackston, 2017). The mechanical effect of pore fluid is readily accounted

54   for by using the effective pressure law (Terzaghi, 1943). The pore fluid acts against the normal stresses acting on crack

55   surfaces hence reducing the shear stress necessary to overcome internal friction of the rocks. Increase in pore pressure

56   during injection can trigger seismicity and therefore pore pressure has to be carefully monitored (Atkinson et al., 2020;

57   Guglielmi et al., 2015). In addition to this mechanical effect, a number of chemical processes can occur in the presence

58   of reactive fluids, leading to complex coupling between processes. For example, the replacement of mafic minerals

59   with carbonates can result in an up to ~44% increase in solid molar volume (Goff and Lackner, 1998; Hansen et al.,

60   2005; Kelemen and Matter, 2008) potentially clogging pore space, reducing permeability and increasing pore pressure.

61   Alternatively, this volume expansion can generate stresses causing reaction-induced fracturing, which provides

62   additional fluid pathways and maintains porosity and permeability for the reaction to proceed (Iyer et al., 2008;

63   Jamtveit et al., 2009; Kelemen & Matter, 2008; Lambart et al., 2018; Macdonald & Fyfe, 1985; Renard et al., 2020;

64   Rudge et al., 2010; Skarbek et al., 2018; Xing et al., 2018; Zhu et al., 2016). The fracturing behavior itself is affected

65   by the fluid chemistry via kinetic reduction of fracture energy due to fluid absorption on mineral surfaces and crack

66   tip blunting (Baud et al., 2000; Orowan, 1944; Rutter, 1972; Scholz, 1968), and activation of fluid-promoted stress

67   corrosion processes such as subcritical crack growth resulting in time-dependent deformation, which is the focus of

Solid Earth

Discussions

68   this paper (Anderson & Grew, 1977; Atkinson, 1984; Atkinson & Meredith, 1987; Brantut et al., 2013; Nara et al.,
69   2013; Rice, 1978).

70   This time-dependent deformation, often called "brittle creep" or "static fatigue", has been observed in all types of
71   rocks tested to date (Atkinson & Meredith, 1987; Brantut et al., 2012; Kranz et al., 1982; Robertson, 1960; Scholz,
72   1968; Zhang et al., 2012). During brittle creep, flaws such as micro-cracks contained in natural rocks are sub-critically
73   stressed and propagate slowly due to stress corrosion (a chemical weakening process) at crack tips in the presence of
74   fluids. Sample-scale fracture then occurs after some time delay when the cracks coalesce and reach a critical length.
75   As a result, the rocks lose their load bearing capabilities and fail along a macroscopic fault plane at stresses well below
76   their short term strength (Scholz, 1972). For the sake of simplicity, we will use creep in the following text to refer to
77   this brittle creep deformation.

78   It has been shown by experiments, observations and modelling that stress corrosion is the dominant mechanism of
79   subcritical crack growth in rocks under upper crustal conditions (Brantut et al., 2012; Michalske and Freiman, 1983;
80   Reber and Pec, 2018). Brittle creep deformation can be accelerated due to changes in the rate of stress corrosion
81   induced by the chemistry of the injected fluids (Renard et al., 2005, 2020) or decelerated by crack tip blunting due to
82   fluid interaction (Scholz, 1968). Overall, it is hypothesized that changes in stress corrosion crack growth rate due to a
83   change in fluid chemistry will be reflected in similar changes of the macroscopic creep strain rate, either accelerating
84   or decelerating based on the details of the ongoing dissolution – precipitation reactions (Brantut et al., 2013). Hence,
85   the effect of CO_2-rich fluids needs to be quantified for GCS applications.

86   To summarize, the influence of rock-fluid interaction on deformation is complicated and includes the coupled effects
87   of mineral dissolution and precipitation, kinetics of fluid assisted deformation and injection pressure built-up, finally
88   resulting in time-dependent rock deformation. Carbonation changes the bulk composition of the basalts, alters their
89   strength and pore structure, and affects the permeability of the rocks (Dunkel et al., 2017; Kanakiya et al., 2017;
90   Kelemen et al., 2013; Kelemen & Hirth, 2012; Lisabeth et al., 2017; Xing et al., 2018; Zhu et al., 2016). Understanding
91   of the effects of rock-fluid interaction on deformation requires dedicated laboratory studies with diverse fluid
92   compositions at in-situ pressure conditions and at elevated temperatures acting over extended timescales. The present
93   study aims at elucidating the effect of rock-fluid interaction on the time-dependent rock deformation by investigating
94   long-term creep of Iceland Basalt saturated with various fluid compositions.

95   **2 Materials and Methods**

96   **2.1 Starting Material and Sample Configuration**

97   We used Iceland Basalt drill cores from the CarbFix site, collected at ~350 m depth. The composition of Iceland Basalt
98   has been identified as tholeiite and contains ~ 25 wt% of calcium, magnesium and iron oxides (7-10 wt% Ca; 5-6 wt%
99   Mg; 7-13 wt% Fe) with an average porosity of ~ 8% based on hydrological and tracer recovery modeling (Alfredsson
100 et al., 2008, 2013; Aradóttir et al., 2012; Matter and Kelemen, 2009; Snæbjörnsdóttir and Gislason, 2016). The rock
101 is formed by an aphanitic matrix that consists of crystals of feldspars, clinopyroxene, iron ore and glass. The fraction
102 of crystal-to-glass ratio as well as crystal habitat is variable as documented in Figure 1. Round pores with a mean

103   diameter of ~ 0.5 mm are randomly distributed throughout the matrix, some are filled with feldspar (primarily

104   potassium feldspar) and some are voids with no filling (Figure 1). Pore-, as well as pre-existing crack-walls are coated

105   by a thin layer of a phyllosilicate as documented in Figure 1d and 1e. The matrix is locally altered by dissolution of

106   larger subhedral feldspar crystals and local replacement by phyllosilicate (see Figure 1b and 1e). Cylindrical samples

107   were ground to ~ 40 mm in diameter and ~ 80 mm in length (see Table 1). The samples were jacketed using copper

108   foil of ~0.05 mm thickness, joined to titanium end-caps by Viton tubes and coated with Duralco 4538 epoxy. The end-

109   caps had a concentric hole which allows fluid access to the sample. Figure 2 shows the schematics of the sample

110   configuration in this study. An internal force gauge was mounted below the sample inside the vessel, allowing direct

111   measurement of the differential stress ($\Delta\sigma = \sigma_1 - \sigma_3$). Displacement of the axial piston was measured externally using

112   a linear variable differential transformer (LVDT). Variations of the sample length were measured using two internal

113   LVDTs. Local axial (ϵ_a) and radial strains (ϵ_r) of the rock were measured using strain gauges affixed to the copper

114   jacket around the sample. Piezoelectric sensors were installed around the sample for passive monitoring of acoustic

115   emissions (AE).
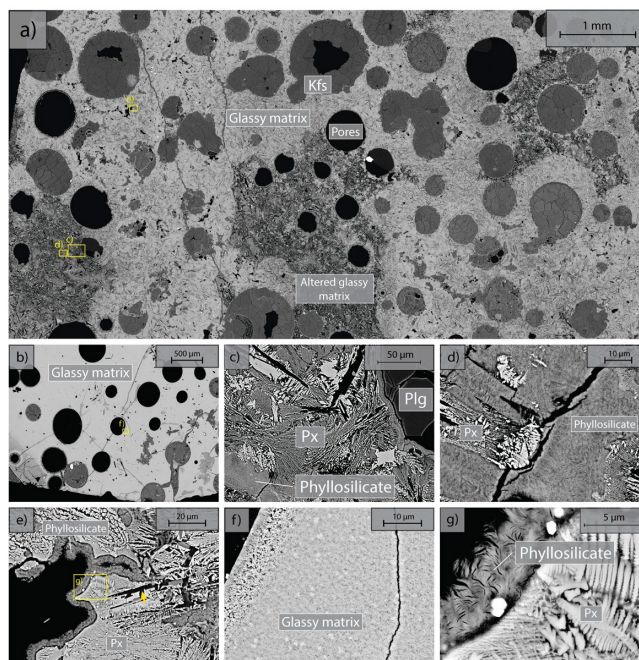
116

117   **Figure 1**. Backscattered electron (BSE) images of the starting material. Location of higher-magnification images is
118   shown by yellow rectangles a) Representative sample microstructure; Glassy matrix shows a range of crystal content
119   and habitat and is locally altered; b) Another common glassy matrix microstructure with finer, more homogenous
120   crystals; c) Detail of altered matrix and pore wall. Note black voids in the shape of subhedral feldspar laths in the
121   matrix; d) Detail of patchy phyllosilicate alteration and dendritic crystals in altered matrix; e) high-magnification
122   image of dendritic crystals forming the matrix and phyllosilicate coating of the pore wall; f) high magnification image
123   of glassy matrix with homogenous small crystals g) high-magnification image of dendritic crystals forming the
124   unaltered matrix and high magnification image of the phyllosilicate alteration.

125 To minimize the issue of inter-sample variability, we adopted the 'stress-stepping' experimental procedures to study

126 creep deformation (Heap et al., 2009; Lockner, 1993). Piezoelectric sensors allowing independent recording of

127 compressional and shear waves were fabricated with PZT-5A ceramics with thickness of ~3 to 5 mm and resonance

128 frequency of ~450 kHz to 1 MHz. The PZT-5A crystals were mounted on titanium spacers with one side concavely

129 curved to match the sample surface, thus providing protection of the sensing crystals and optimal contact area. A back-

130 up element was epoxied to the back of the sensor to minimize ringing. We also used analog low pass filters (~500

131 kHz) compatible with the frequency range of the employed PZT ceramics to reduce the electromagnetic interference

132 (EMI) effect. Data was collected using two combined 4-channel universal serial bus (USB) oscilloscopes, recording

133 at 50 MS/s with a 12-bit resolution (TiePie HS4-50). Using low noise amplifiers (ITASCA-60dB), we carefully

134 selected the most sensitive sensor positions, preferably far from each other, as master channels. The data collection

135 system was set such that, if the master channels detected a signal satisfying a sufficiently large signal/noise ratio in a

136 moving time window, the event would be recorded in all channels. We amplified the two master channels with a flat

137 gain of 60 dB in a frequency range of 50 kHz to 1.5 MHz. Frequencies from 1.5 MHz to 15 MHz were amplified

138 nonlinearly, the gain decreasing exponentially from 52 dB to 37 dB with increasing frequency (Ghaffari and Pec,

139 2020). Considering the above limitations, the main frequency range of the recording system was between ~50 and

140 500kHz, although other frequencies could be recorded owing to the exponential nature of the amplification filters.

141
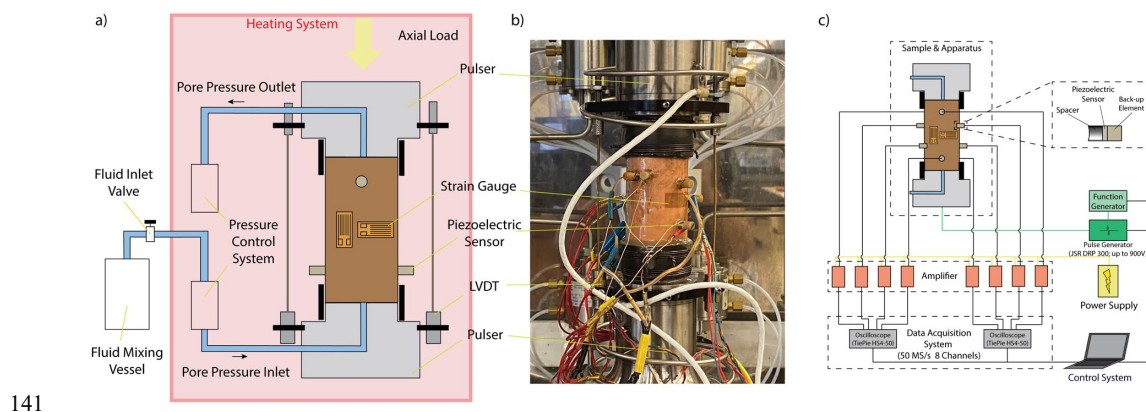
Figure 2. a) Schematics of sample configuration. The whole sample assembly and pore fluid actuators are enclosed in a servo-controlled heating system to ensure a uniform temperature condition; b) Photo of the sample assembly; c) Illustration of the acoustic emission recording system.

2.2 Experimental Setup and Analytical Methods

146 All experiments were conducted at 50 MPa effective pressure, P_{eff}, with pore fluid pressures, P_f, of either 0 or 5 MPa

147 for dry and fluid-saturated experiments, respectively. The fluids used in this study were H_2O and H_2O+CO_2. The fluid-

148 saturated samples were first immersed in deionized water under vacuum for more than 30 days prior to the experiment.

149 Details of the experimental conditions are listed in Table 1. The samples were inserted in the NER Autolab 3000

150 testing rig installed at MIT and deformed under tri-axial stress conditions, with the maximum principal stress (σ_1)

151 acting in the axial direction. The radial principal stresses (σ_2 and σ_3) were generated by the confining pressure, i.e.,

152 $\sigma_2 = \sigma_3 = P_c$. The effective pressure is calculated as $P_{eff} = P_c - P_f$. During deformation, a constant pressure difference

153   of 0.5 MPa was maintained between the inlet and outlet of the pore pressure system, while the mean pore pressure

154   was kept at 5 MPa. We thus maintained fluid flow across the sample and measured the permeability evolution during

155   deformation. In one H_2O+CO_2 experiment (OR2_M), we closed the fluid mixing vessel after the initial filling of the

156   sample and thus formed a close pore fluid loop (OR2_M was referred to as H_2O+CO_2 close experiment in the following

157   discussion). In the other H_2O+CO_2 experiment (OR3_B), the pore fluid system was connected to the fluid mixing

158   vessel during the entire experiment and therefore acted as a semi-open system since it was in constant communication

159   with a large CO_2 source (OR3_B was referred to as H_2O+CO_2 open experiment in the following discussion).

Experiment Number	Sample Length (mm)	Sample Diameter (mm)	Confining Pressure (MPa)	Pore Pressure (MPa)	Effective Pressure (MPa)	Pore Fluid Composition	Temperature (˚C)	Young's Modulus (GPa)	Ultimate Strength (MPa)	Strain at Failure (%)	Initial Porosity (%)
OR5	77.37	39.32	50	0		-		17.6	>105	1.89	15
OR2_T	81.5	38.01	55	5		H_2O		12.1	72	1.71	11
OR2_M	81.48	39.22	55	5	50	$H_2O + CO_2$	78	16.2	55	0.84	5
OR3_B	77.94	39.81	55	5		$H_2O + CO_2$		28.0	130	2.00	-

160   **Table 1.** Details of the sample parameters and experimental conditions. Sample OR5 was not loaded to its ultimate
161   strength due to early failure of the strain gauges and LVDTs. Porosity is estimated from the X-ray tomographic image
162   of the sample. Initial porosity of the sample OR3_B is not available due to limited access to the X-ray tomography
163   facility during COVID-19 pandemic.

164   We started the experiments by bringing the sample to an effective pressure of 50 MPa and subsequently to a

165   temperature of ~80˚C while holding the pressure constant. Heating the sample took ~12 hours, long enough to allow

166   thermal equilibrium to be reached. After reaching the desired P - T conditions, the samples were deformed using a

167   step loading procedure. During a step, the load was increased at a rate of ~2 MPa/min, which corresponds to an axial

168   strain rate of ~1.1×10^{-6} s^{-1}. Once the desired stress level was reached, we kept the load constant for ~24 hours, while

169   monitoring the sample deformation. This sequence was repeated as many times as desired for the next loading steps.

170   The total duration of the experiments ranged between 5 to 12 days. Details of the load steps are summarized in

171   Appendix (Figure A1).

172   In this study, we use the term phase I to refer to the creep immediately following a stress change, during which strain

173   evolves rapidly. We call phase II the portion of the creep curve with an approximately constant or very slowly varying

174   strain rate over a ~24h window (i.e. $d\varepsilon/dt = cte$.; see Appendix Figure A2). For comparison with previous work on

175   brittle creep, we calculate a characteristic creep strain rate using a least-squares fit to the slope of the creep strain vs.

176   time curve during the identified phase II transient creep (Appendix Figure A4; we will simply refer to it as creep rate

177   in the following discussion).

178   To investigate the micro-structural changes occurring during deformation, the rock samples were scanned before and

179   after deformation using X-ray computed tomography with scan parameters set at ~150 kV and ~250 µA. The obtained

180   X-ray images have a pixel size of ~90×90 µm. Thin sections were prepared from selected samples and imaged using

181   a field emission scanning electron microscope (SEM).

182   The evolution of fluid composition was evaluated by collecting fluid samples from the end of the pore fluid outlet

183   (Figure 2a) after each creep step. The concentration of Mg^{2+}, Ca^{2+} in the fluid sample were analyzed using the

184   Inductively Coupled Plasma Mass Spectrometry (ICP-MS).

185   **3 Results**

186   **3.1 Creep Deformation and Creep Strain Rate**

187   The creep deformation during each load step exhibited typical transient creep evolution (Brantut et al., 2013;

188   Robertson, 1964; Scholz, 1968) with a transition from rapidly evolving phase I to slowly varying phase II (Figure 3).

189   This transition generally took place within the first 10^4 s (~2.7 hrs) of the loading step. In the dry experiment, large

190   variations in phase I creep strains were observed (Figure 3a & 4c) and the creep rates measured during the slowly

191   evolving phase II stages showed a weakly negative sensitivity to stress (Figure 3e). In experiments where pore fluids

192   were present (H_2O and H_2O+CO_2), the strain accumulated during the phase I creep systematically increased with

193   increasing stress and the creep strain rate displayed a clear exponential dependence on stress (Figure 3e). This stress

194   sensitivity of creep strain rate showed strong similarity in the different experiments irrespective of the pore fluid

195   composition and can be adequately described by power law (e.g. Atkinson, 1984; Meredith and Atkinson, 1983) as

196   well as exponential functionals (Charles and Hillig, 1962; Hillig, 2006), but the exponential model seems to work

197   slightly better with our data according to the R^2 value (see Appendix Figure A5).

198
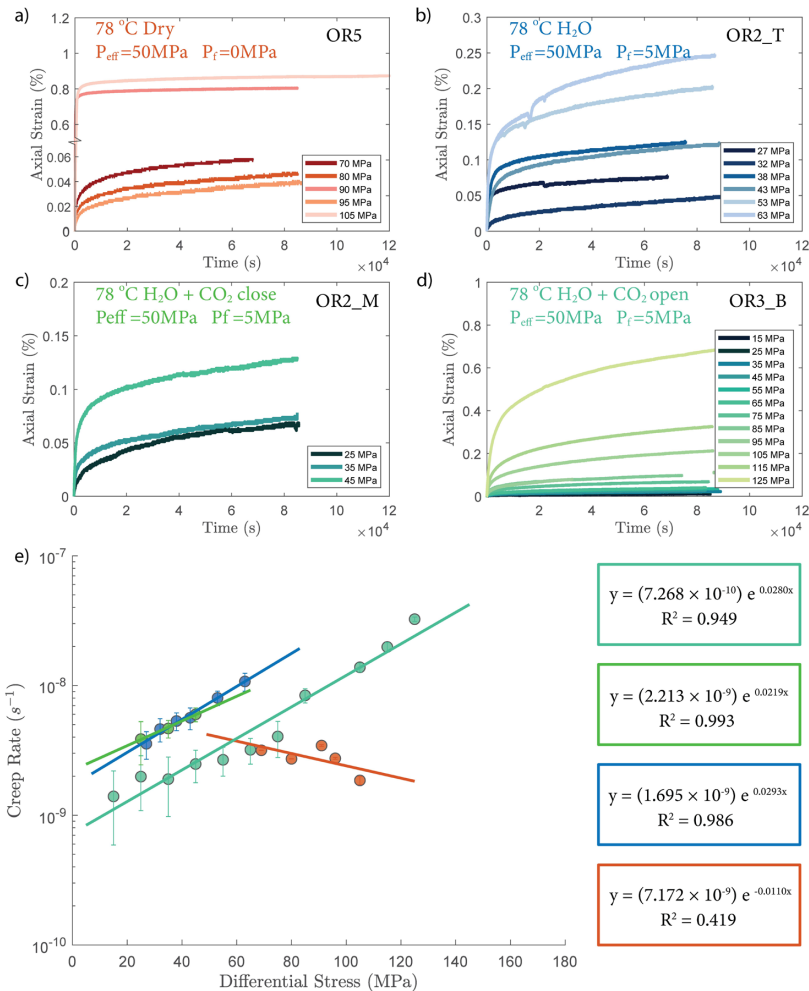
Figure 3. a) - d) Axial strain evolution of each individual stress steps for all experiments; e) Stress dependence of creep rate. The error bar marks the 95% confidence interval of the calculated creep rates. The stress-creep rate relationship can be best modeled using an exponential law.

In Figure 4 we compare the strain accumulation during phase I and II of the transient creep as illustrated in Figure A4a. We observe a universal power-law relationship of the accumulated creep strain during phase I to that measured at an arbitrary observation time of ~24 hrs after the stress step loading during phase II, in all experiments irrespective of fluid presence or the composition of the fluid (Figure 4a). The accumulated creep strains during both phase I and phase II were exponentially dependent on creep stress (Figure 4c and 4d). In Figure 4b we show that regardless of the creep stress level, the ratio between the logarithmic accumulated phase I and logarithmic phase II creep strain after ~24 hrs was approximately constant, except for two outliers associated with two stress steps in the dry experiment, during which anomalously large phase I creep strains occurred (Figure 4a and 4c).

210 Overall, the fluid saturated samples crept faster than the dry sample during phase II stages in similar stress conditions.

211 In spite of variations in ultimate strength, the fluid saturated samples consistently showed stronger stress dependence

212 of the creep rate than the dry sample. Comparing the fluid saturated experiments, we observe that the sample saturated

213 with H_2O had the same creep rate as the $H_2O + CO_2$ close experiment and a higher creep rate than the H_2O+CO_2 open

214 experiment under similar stress level. (Figure 3e). Analysis of the fluid chemistry demonstrates that the $H_2O + CO_2$

215 close and H_2O experiment show same fluid composition which we will describe in more detail in Section 3.6.
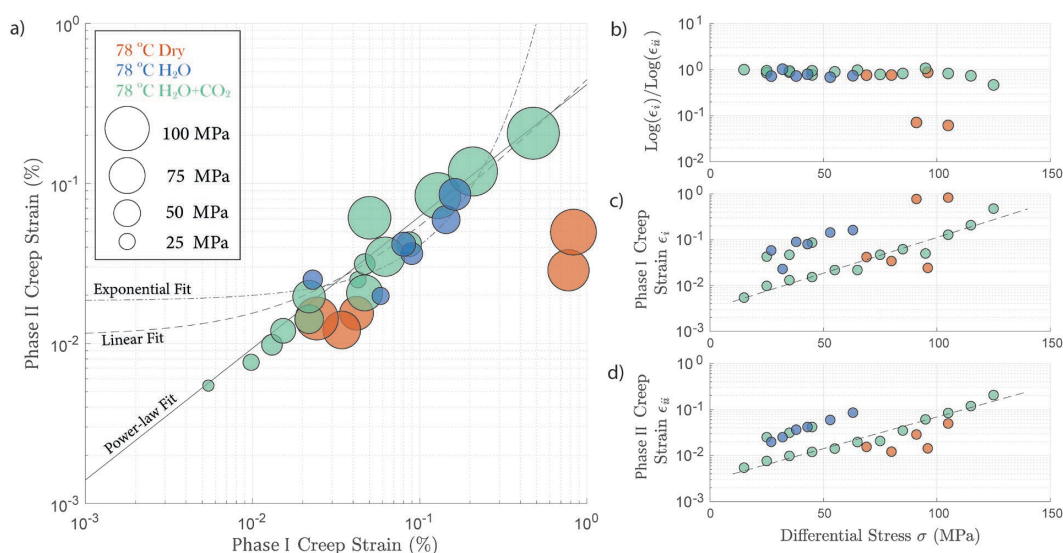
216

Figure 4. a) Relationship between total phase I creep strain and phase II creep strain ~24 hrs after the stress step
loading. The creep stress level is reflected by the size of the circles; b) ratio between the logarithmic total phase I and
logarithmic phase II creep strain remains constant and is independent of stress; the cumulated c) phase I and d) phase
II creep strain is exponentially dependent on the creep stress; The fitted lines are calculated based on the data obtained
from $H_2O + CO_2$ open experiment (OR3_M).

3.2 Volumetric Strain

223 In all experiments, creep deformation was initially compressive as indicated by a positive change in the volumetric

224 strain, ϵ_v, calculated from the strain gauge measurements ($\epsilon_v = \epsilon_a + 2\epsilon_r$). Shear-enhanced dilation (Brace et al., 1966)

225 started 10 - 20 MPa before the ultimate strength of the sample was reached (highlighted by yellow arrowheads in

226 Figure 5). The onset of dilation generally occurred at lower stress level in the fluid saturated experiments than in dry

227 conditions. The largest dilation was observed in H_2O+CO_2 open experiments as shown in Figure 5d. In the dry

228 experiment, large amount of dilation ($\Delta\epsilon_v > 0.5\%$) was also observed at creep stress of ~90 MPa and ~105 MPa which

229 is significantly higher than in other steps ($\Delta\epsilon_v < 0.1\%$). Furthermore, the dilation at ~90 MPa is also accompanied by

230 a drop in stress (see Figure 5). The strength of the tested samples seems to be correlated with the elastic modulus

231 measurements, the stiffer the rock the higher the strength (see Table 1).
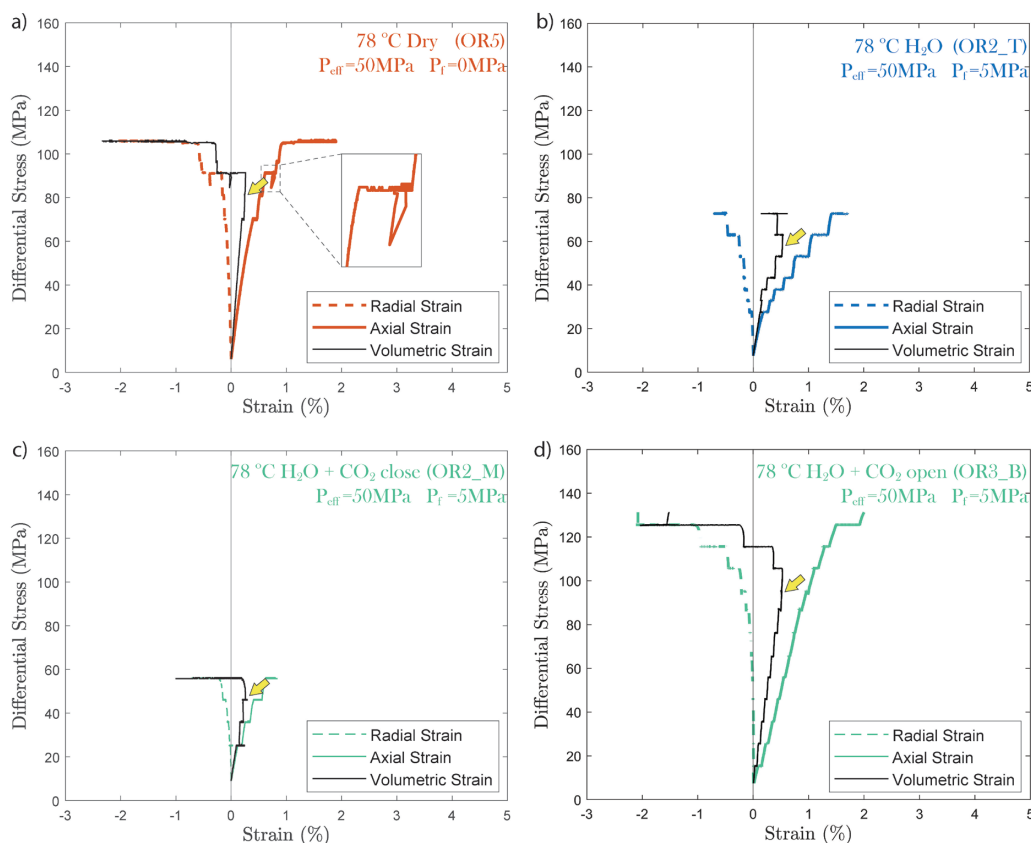
Figure 5. Plots of volumetric strain for a) dry, b) H_2O, c) H_2O+CO_2 close and d) H_2O+CO_2 open experiments. The onset of dilatancy is marked by the yellow arrowhead. In the dry experiment, the differential stress exhibits temporary fluctuation at ~90 MPa (highlighted by the dashed rectangle).

3.3 Permeability

In fluid-saturated experiments, permeability decreased with increasing effective pressure during hydrostatic loading (Figure 6a, b and c). The largest decrease in permeability was observed in the water-saturated experiment, where permeability dropped by 3 orders of magnitude as effective pressure was raised from 15 to 50 MPa (Figure 6a). Permeability reduction was much lower in both H_2O+CO_2 experiments, only ~ 1 order of magnitude, over the same effective pressure range (Figure 6bc). Permeability variations after heating are shown in Figure 6d 6e and 6f, where the minimum permeability reached during hydrostatic loading is indicated for comparison (empty circles in Figure 6d, e and f). The permeability change during heating was rather small in the H_2O and H_2O+CO_2 close experiment, while the H_2O+CO_2 open experiment exhibited more than an order of magnitude permeability reduction after heating.

During creep, permeability did not evolve much with time but did show a clear dependence with the stress level of the individual creep stages, first slightly decreasing with increasing differential stress and then substantially increasing when the onset of shear-enhanced dilation was passed, shortly before failure (Figure 6d and 6f).
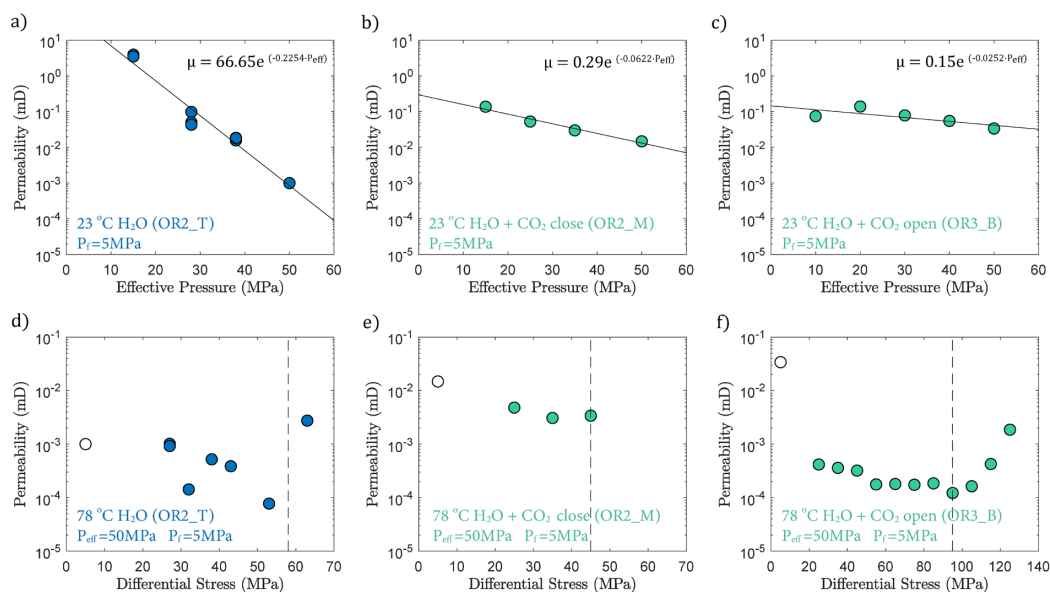
Figure 6. Permeability evolution due to changes in a) b) c) effective pressure and d) e) f) differential stress. The dash-line marks the onset of shear-enhanced dilation as previously shown in Figure 4. The empty circle indicates the permeability measurement before heating.

3.4 Characterization of the Acoustic Emissions

3.4.1 Passive Recording & Rate of AEs

We observed a strong correlation between acoustic emissions and mechanical data as documented in Figure 7. The number and amplitude of AEs was substantially larger in the experiments with pore fluids than in the dry experiment, irrespective of fluid composition. The rate of AEs increased during primary creep; the greater the accommodated strain was, the higher the AE rate. The AE rate then decayed exponentially as the rock entered the later stage of the transient creep. This decay was slower in all fluid saturated experiments where significant amount of AE activity continued during the phase II creep stage. The AE rate increased as the stress was approaching the ultimate strength of the sample (Figure 7). In Figure 8, we plot the normalized cumulative AE counts against the normalized creep strain measured during each creep step. For all experiments with pore fluids, we see that the data-points tended to cluster near the 0-1 diagonal (Figure 8b, c and d), thus supporting a strong correlation between acoustic emissions and creep strain. In the dry experiment, most AEs occurred early in each load step (normalized strain ≤ 0.2) after which straining continued with little AE activity (Figure 8a).
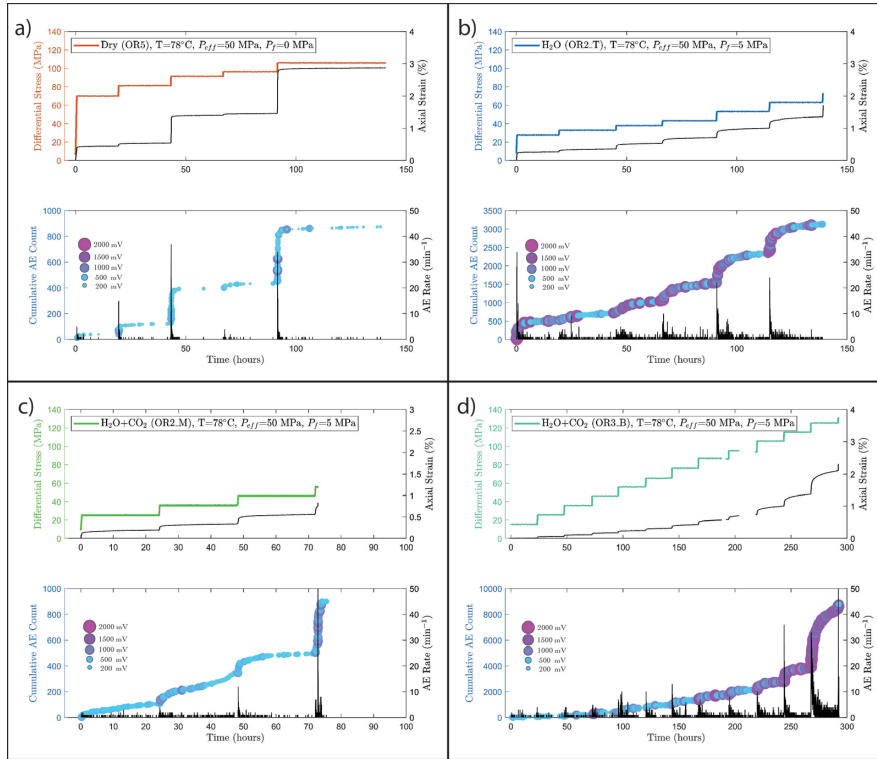
Figure 7. Top: Plot of stress loading steps and strain (black) evolution; Bottom: Evolution of cumulative number of acoustic emission (AE) and AE rate evolution (black) over time for a) dry, b) H_2O, c) H_2O+CO_2 close and d) H_2O+CO_2 open experiments.
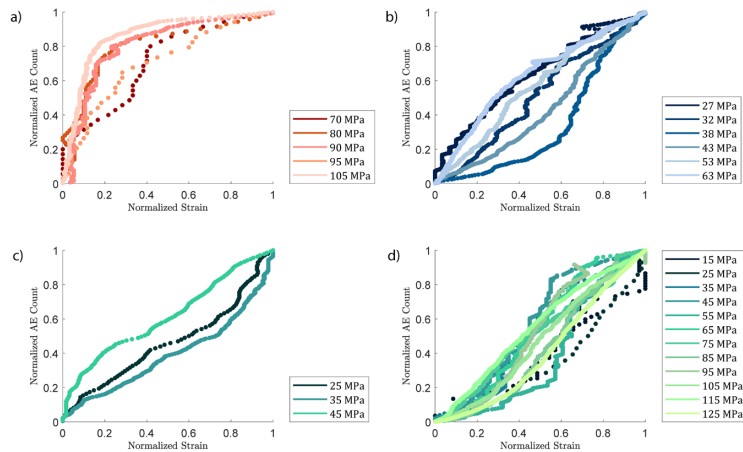
Figure 8. Plot of normalized cumulative AE count vs strain a) dry, b) H_2O, c) H_2O+CO_2 close and d) H_2O+CO_2 open experiments. the normalized cumulative AE counts and strain during each creep step show an approximately linear correlation in most cases except in the dry experiment.
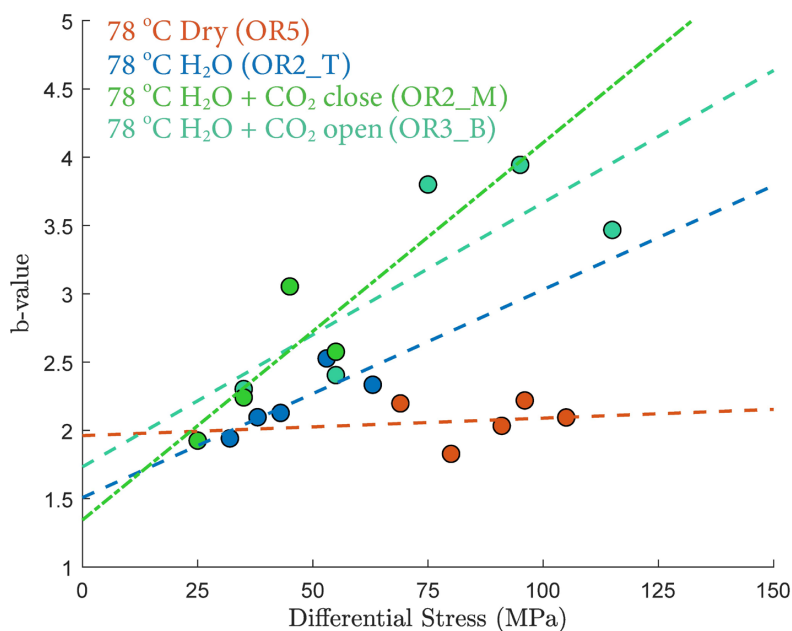
3.4.2 Gutenberg-Richter b-value

The Gutenberg-Richter relationship provides a way to characterize the AE statistics for each creep step. The Gutenberg-Richter b-value was calculated using the following equation:

$$\log N = a - b \log A \qquad \text{(Eq. 7)}$$

where A is the maximal amplitude of individual acoustic events and N is the number of events with magnitude larger than A. Figure 9 shows that the b-value increased with increasing stress in the fluid saturated experiments but remained constant in the dry experiment. The observed increases of the b-values indicate that low amplitude AEs had a proportionally larger frequency with increasing stress.


Figure 9. Differential stress dependence of Gutenberg-Richter b-values. See detailed b-value fitting in the Appendix Figure A6.

3.5 Microstructure

Post-mortem examination of the samples reveals that fractures inside the fluid-saturated samples form a complex, wide system rather than a clearly defined, distinct shear fault plane (Figure 10 and Appendix Figure A7). The fluid-saturated samples exhibit bulging on the surface. In contrast, the dry sample shows a weakly developed fault plane and less bulging, however it should be noted that this sample did not, in fact, reach ultimate strength.

Solid Earth
Discussions
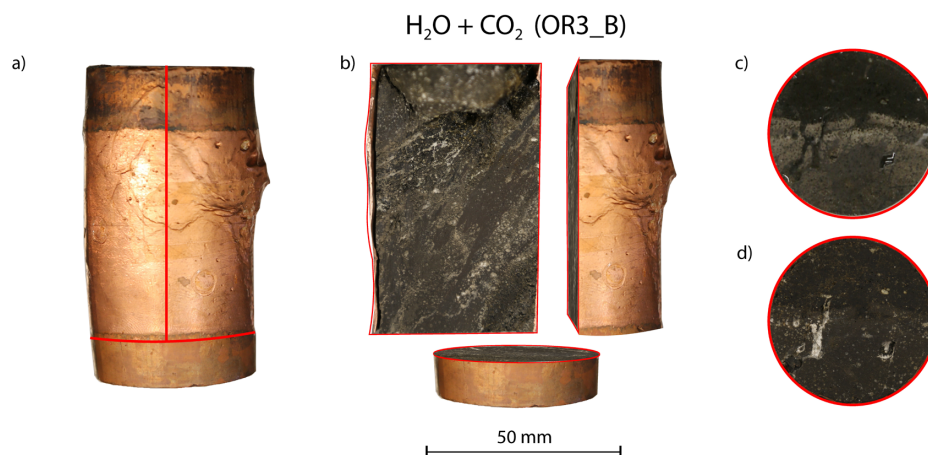
$H_2O + CO_2$ (OR3_B)

Figure 10. a) Deformed sample from H_2O+CO_2 open experiment (OR3_B). b) Cross-sectional view of the deformed sample. Top view of the sample c) before and d) after the experiment.

X-ray tomographic images (Figure 11) and BSE images (Figure 12) of the deformed samples display abundant fractures, whereas cracks are much more rare in the pre-deformation CT scans and the BSE images (Figure 1). The amount of visible cracks in each sample tends to scale with the cumulative AE count; the dry experiment has a lower fracture density than the experiments with H_2O and $H_2O + CO_2$ despite the fact that the dry sample experienced a higher stress and developed a larger total strain accumulation. To illustrate these observations, we selected representative pairs of 2D tomographic slices oriented parallel and perpendicular to the loading direction and traced the observable microcracks (Figure 11). We quantified both the orientation and anisotropy of the microcracks using the 'surfor' method that relies on the projection of an outline (Heilbronner and Barrett, 2014; Panozzo, 1984). As documented in Figure 11, cracks are strongly aligned in the axial sections. The cracks are mainly oriented parallel to the maximum principal stress in the H_2O+CO_2 experiment, indicating Mode I cracking, but are aligned 20~30° to the maximum principal stress in the dry and H_2O experiments, suggesting mixed Mode I + Mode II cracking. A weaker alignment is generally observed in radial sections.

3.6 Fluid Chemistry

Concentration of the Mg^{2+} and Ca^{2+} cations increased once heating started (Figure 13). This increase in the Mg^{2+} and Ca^{2+} concentration reflects the dissolution of Mg and Ca bearing minerals during the reaction. In the H_2O+CO_2 close experiment (OR2_M), the supply of CO_2 was limited and led to a dissolution dominated system that resulted in the high concentration of Mg^{2+} and Ca^{2+}, similar to the H_2O experiment (OR2_T). In the H_2O+CO_2 open experiment (OR3_B), the cation concentration was significantly lower than in the OR2_M and OR2_T experiments. This was likely caused by the potential precipitation uptake owing to the continuous supply of CO_2 in the semi-open setting of the pore fluid system. This interpretation is also supported by the ~2 orders of magnitude drop in permeability observed in the CO_2 open experiment after heating started since precipitation could potentially clog the pore throats and lead to permeability decrease.

14
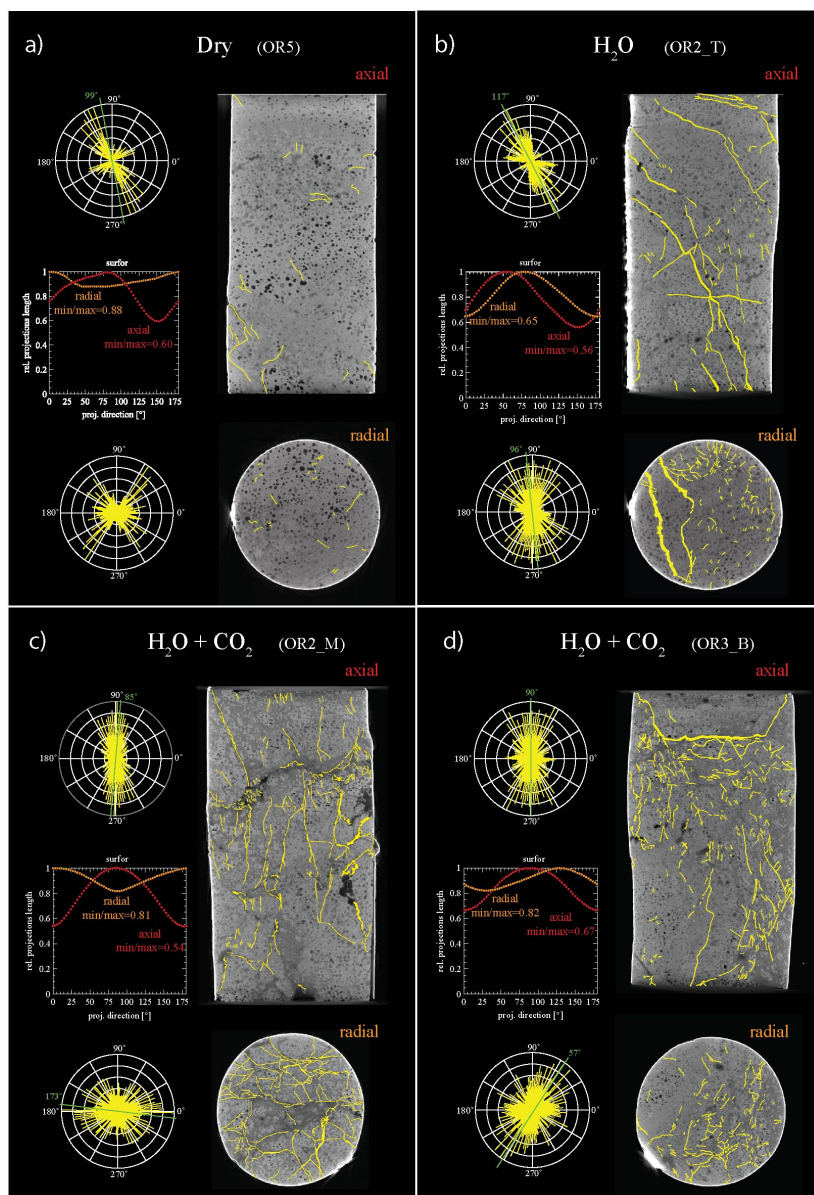
Figure 11. Orientation analysis of cracks in axial and radial directions from x-ray tomographic images of the deformed sample from a) dry, b) H_2O, c) H_2O+CO_2 close and d) H_2O+CO_2 open experiments. The aspect ratio (min/max), which is defined by the ratio between the minimum and maximum projection length of the cracks, is 1 when the orientation is random (isotropic) (Heilbronner and Barrett, 2014). Strong crack alignment is inferred in the axial sections with aspect ratio of 0.5~0.7 compared to the radial sections where the aspect ratio is 0.6~0.9.
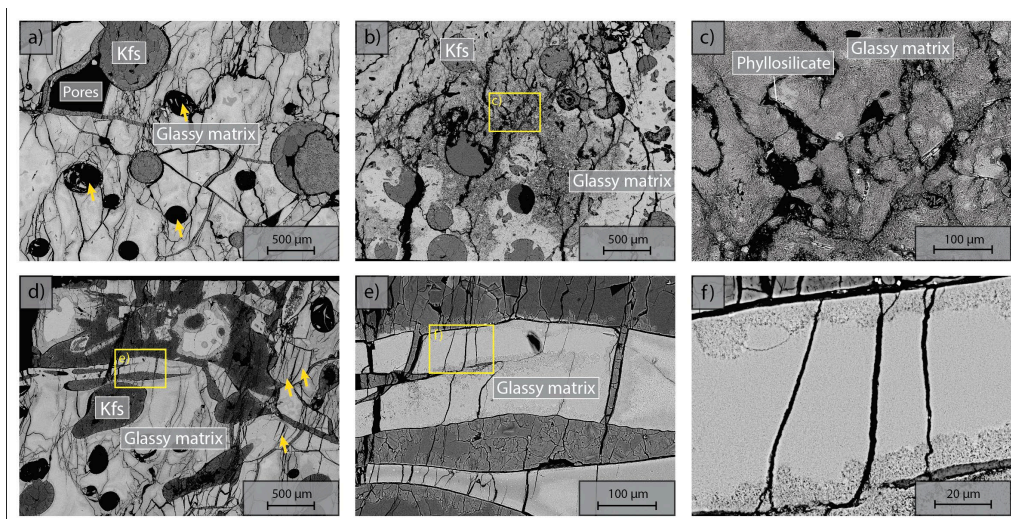
Figure 12. Microstructures of deformed sample from H_2O+CO_2 open experiment (OR3_B). Axial view, loading from top and bottom. a) Pervasively fractured matrix, note the preferential N-S alignment of cracks indicating most cracks are mode I. Note the collapse of void pores with cracks emanating (arrows). b) Crack pattern in altered glass matrix. c) close up of b). Note the phyllosilicate coating on the crack wall. d - f) magnification cascade illustrating the crack shape and morphology in the deformed sample.
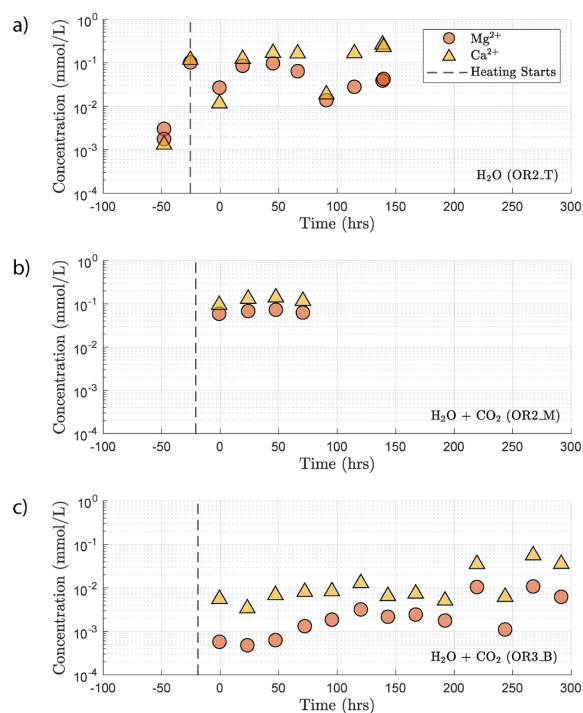
Figure 13. Concentration of Mg^{2+} and Ca^{2+} in the sampled fluid from a) H_2O, b) H_2O+CO_2 close and c) H_2O+CO_2 open experiments. Time 0 marks the start of the first creep stepping.

4. Discussion

4.1 Active Deformation Mechanisms

Acoustic emission, microstructure analysis and mechanical data confirm that the observed deformation is a brittle process as is expected at the given P-T conditions. The strong similarity between the time evolution of cumulative AE counts and strain (Figure 7 and 8) is consistent with observations from other creep deformation experiments using cemented and uncemented porous rocks (e.g. Brzesowsky et al., 2014; Heap et al., 2009). These considerations suggest that the creep deformation observed in this study is a result of a time-dependent brittle process such as subcritical cracking, that can still generate AE activity (Chester et al., 2007; Chester et al., 2004).

Previous studies concluded that brittle creep is unlikely to occur below the onset of dilatant cracking (C') that is expected at about 80% of ultimate failure strength (Baud & Meredith, 1997; Heap et al., 2009). However, all our strain measurements (strain gauges, LVDTs, axial ram displacement) show that, in this study, creep did occur at stress levels of only ~11% of ultimate failure strength, well below C'. Similar creep deformation with measurable strain at low stress level has been previously observed in shale (e.g. Mighani et al., 2019). It can be argued that such low-stress creep deformation is associated to shear-enhanced compaction instead of dilatant cracking and that a change of mechanism may take place at C' (Vajdova et al., 2012; Zhu et al., 2010). However, we found that the strain rates measured during the creep steps below C' could be fitted using the same exponential law derived from strain rate measurements above C'. Furthermore, the amount of creep strain accumulated during phase I and phase II showed a consistent stress dependence across all stress conditions (Figure 4c and 4d). Therefore, the creep deformation above and below the point of dilation (C') was likely governed by the same mechanism, and the accumulated creep strain at a given time can be formulated as a function of stress.

Our AE statistics show that the b-values were higher for the fluid-saturated experiments than the dry experiment, indicating a higher proportion of low amplitude AEs (i.e., higher ratio of low-to-high amplitude events). This abundance of low amplitude events in fluid-saturated rock is a direct evidence that aqueous fluids promoted creep deformation in basalt. As argued in previous studies, growth of small cracks and low amplitude events are facilitated when stress corrosion is activated in the presence of aqueous fluids (Hatton et al., 1993). We also observed that the amplitude of the largest events increased with increasing stress. This could be attributed to the increase in micro-crack nucleation, consequently maximizing the likelihood of an 'avalanche' of coalescing cracks, which, in turn, generates large amplitude events. Overall, as more and more energy is dissipated through micro-cracking and the associated low amplitude AEs, the macroscopic deformation becomes less dynamic, which is consistent with the increase in the Gutenberg-Richter b-value with increasing stress.

Post-mortem examination of the fluid-saturated samples demonstrated the presence of a complicated network of fractures within the sample and absence of a well-defined major shear fracture plane. The samples also exhibited dilation features such as bulging, likely caused by the bulk formation of dilation cracks. These microstructural observations further support the idea that deformation during creep is diffuse and distributed rather than localized (Hatton et al., 1993; Heap et al., 2009), consistent with nucleation-controlled crack growth since the nucleation sites are normally randomly distributed in the sample.

365   Microstructure analysis of the deformed samples demonstrates that the presence of fluid resulted in more abundant

366   mode I cracks (Figure 11). Larger amount of cracks oriented parallel to the maximum principal stress were observed

367   in the H_2O+CO_2 samples, implying dominant Mode I cracking, while the dry experiment showed less cracking, with

368   the cracks aligned 20-30° to the maximum principal stress, thus pointing to mixed Mode I + Mode II cracking. This

369   observation is consistent with previous studies on strain localization as they often proposed rock fracture models

370   predicting that mode II cracking takes place during the localization stage of fracture development (Lockner et al.,

371   1992; Reches and Lockner, 1994; Wong and Einstein, 2009). Among the present experiments, the samples subjected

372   to creep deformation under H_2O+CO_2 conditions exhibited the largest amount of mode I cracks. The sample deformed

373   under dry condition, despite having experienced similar differential stress and total accumulated strain, showed a

374   lower amount of cracks. As stated in previous studies, mode II cracks often propagate at velocities close to the

375   Rayleigh velocity, which increases the probability of occurrence of high amplitude events. On the other hand, mode I

376   cracks have significantly lower rupture velocities and tend to produce low amplitude acoustic events (Broberg, 2006).

377   Therefore, increased mode I cracking should lead to an increase in the proportion of low amplitude AEs, i.e. an

378   increase in the Gutenberg-Richter *b*-value.

379   We infer that the difference in creep rate of the dry and fluid-saturated experiments is a result of fluid-assisted

380   subcritical crack growth. The fluid presence promotes stress corrosion, possibly related to hydrolytic weakening

381   (Atkinson, 1984), accelerates crack growth, activates more crack nucleation sites, and, consequently, leads to a

382   distributed array of small micro-cracks. In contrast, crack growth under dry conditions is concentrated on fewer and

383   larger cracks since activation of the nucleation sites is more difficult. Thus, it is easier to create localized deformation

384   under dry condition.

385   Previous studies also suggested that intergranular pressure solution (IPS) could play a significant role as a deformation

386   mechanism during creep (Liteanu et al., 2012; Zhang & Spiers, 2005; Zhang et al., 2010). The creep deformation by

387   IPS involves dissolution and the presence of a fluid phase might be expected to affect creep deformation, generating

388   additional strain accumulation apart from dilatant cracking. Importantly, because the driving process of IPS is not

389   producing abrupt stress drops, it is not expected to produce acoustic emissions. Although we did see difference in

390   creep strain between the dry and fluid-saturated experiments, it was likely caused by dynamic fracturing, as evidenced

391   by the volumetric strain and AE observations (Figure 5a and A1). We attribute the change in creep strain rate between

392   dry and fluid-saturated experiments to fluid-assisted subcritical crack growth. We posit that under our experimental

393   conditions, IPS was not a dominant creep mechanism, however more detailed microstructural observations are needed.

394   **4.2 Time and Stress Dependent Deformation**

395   Our experiments show that the time-dependent creep deformation was also strongly stress dependent. We observed

396   that the creep strain accumulated during phase I was exponentially dependent on stress (Figure 3c). Two exceptions

397   are noted in the dry experiment. Both showed high strain accumulation during phase I transient creep and followed a

398   sharp temporary stress drop during the creep step with a nominal differential stress of ~90 MPa (Figure 5). This

399   temporary stress drop was accompanied by a swarm of large amplitude AEs (Appendix Figure A1), implying that the

400   concurrent strong dilation was likely caused by local dynamic fracturing while the bulk of the sample remained mostly

401   intact and still capable of supporting the applied load.

402   We also observed an exponential relationship between stress and creep rate. Interestingly, the fluid-saturated

403   experiments yielded approximately equal stress sensitivities of the creep rates, $\dot{\varepsilon} \propto e^{0.02 \sim 0.03\,\sigma}$, despite the variability

404   in their absolute strengths (Figure 3). The exponential stress dependence of strain rate in fluid-saturated experiments

405   is consistent with brittle creep being the dominant deformation mechanism. Indeed, the values of the fitting constant

406   (0.02~0.03) are comparable in order of magnitude to those reported in previous studies on other basaltic rocks (0.05

407   in Heap et al., 2011, from experiments using Etna Basalt). Since the creep rate was exponentially dependent on stress,

408   so should be the accumulated phase II creep strain. This inference is supported by our observation in Figure 4d.

409   Concerning the dry experiment, we attribute the slightly negative dependence of creep strain rate on stress (Figure 3e)

410   to damage-related strain hardening. However, it is also possible that this observed negative dependence was only a

411   statistical artefact owing to large data fluctuations as suggested by the low R^2 value of the exponential fitting

412   (Appendix Figure A5).

413   The fact that both cumulative phase I and phase II creep strains were exponentially dependent on stress (Figure 4c and

414   4d) implies a power-law relationship between the accumulated phase I and phase II creep strain, which is independent

415   of the stress level and even the presence or absence of fluids. This empirical relationship can be formulated as:

416
$$\frac{\log\left(\varepsilon_t - \varepsilon_i\right)}{\log\left(\varepsilon_i\right)} = \frac{\log\left(\varepsilon_{ii}\right)}{\log\left(\varepsilon_i\right)} = cte. \tag{Eq. 8}$$

417   where ε_t is the total strain accumulated at the end of an individual creep stage (~24 hrs), ε_i the creep strain accumulated

418   during phase I, and ε_{ii} the strain accumulated during phase II (see Appendix Figure A3). This phenomenological

419   power-law relationship is supported by our observation that the ratios in Equation 8 were indeed approximately

420   constant ~0.8 (Figure 4a and 4b). This power-law relationship expressed in Equation 8 implies that the strain evolution

421   with time can be predicted; some fundamental link between strain accommodated in phase I creep and strain rate in

422   phase II creep exists.

423   **4.3 Fluid Chemistry Evolution and Influence of Fluid Composition**

424   The increase in concentration of both Mg^{2+} and Ca^{2+} occurring after heating in the H_2O and H_2O+CO_2 close experiment

425   (Figure 14) indicates that the system was dominated by dissolution of Mg and Ca bearing minerals. In the case of the

426   H_2O+CO_2 open experiment, we observed a much smaller increase in cation concentration implying that a significant

427   amount of the released Mg^{2+} and Ca^{2+} cations reacted with the continuously supplied CO_2 in the semi-open setting to

428   form carbonate precipitates. These cation concentration trends appeared strongly correlated with the permeability

429   evolution and creep strength of the rocks. The experiment with H_2O+CO_2 open showed a larger post-heating

430   permeability decrease than the experiments with H_2O and $H_2O + CO_2$ close and was stronger (Figures 3e and 6). The

431   absolute creep rate was consistent for experiments with comparable fluid chemistry (H_2O and $H_2O + CO_2$ closed) and

432   about a factor of 3 faster than in the experiment where precipitation was dominant ($H_2O + CO_2$ open) indicating that

433   precipitation reactions slightly strengthen the rock. This congruence of observations is a strong argument that

434   precipitation occurred in the pore space of the CO_2 open experiment. However, we could not directly resolve evidence

435   of precipitation within the resolution of our microstructural observations and this requires further study. Interestingly,

436   the strain rate sensitivity to stress was similar in all fluid-saturated experiments (Figure 3), implying that creep rate

437   sensitivity to stress was not significantly influenced by the fluid chemistry.

438   Our chemical data support the idea that carbonation of basalt is a kinetically favored reaction and are consistent with

439   the fast rate of carbonation observed during the CarbFix field tests (Matter et al., 2016). The difference between the

440   Mg^{2+} and Ca^{2+} concentrations measured in the H_2O+CO_2 open experiment and those in the H_2O and H_2O+CO_2 close

441   experiments indicates that the rate-limiting factor during carbonation under our experimental condition was the net

442   supply of Mg^{2+} and Ca^{2+} cations, which is associated with dissolution and is reduced when precipitation occurs.

443   **4.4 Permeability & Porosity Evolution**

444   Permeability was affected by both chemical and mechanical processes. The evolution of permeability during the

445   experiments was generally consistent with previous observations of monotonic permeability decrease during

446   hydrostatic loading of samples of limestone, sandstone and Etna basalt (Brantut, 2015; Fortin et al., 2011; Zhu &

447   Wong, 1997). Comparison of the dissolution dominated experiments (H_2O and H_2O+CO_2 close) and the precipitation

448   dominated experiment (H_2O+CO_2 open) shows that the carbonation reaction reduced permeability in our experiment.

449   In low differential stress conditions, the samples compacted and this compaction was accompanied by a further

450   permeability decrease, which was likely related to the pore volume reduction expected during compressive

451   deformation. Shortly before ultimate strength was reached, volumetric dilation became dominant and coincided with

452   permeability increase. Our observations of the permeability evolution demonstrate that, although the permeability

453   might decrease owing to compaction, formation and propagation of cracks can mitigate the permeability loss and even

454   lead to an increase with further cracking. The effect of creep deformation on the long-term permeability evolution of

455   reservoir rocks is therefore non-negligible. Increase in permeability, combined with other observations such as

456   increasing volumetric strain and acoustic emissions, could potentially be used as a warning sign for impending failure

457   during the long-term monitoring of reservoirs' integrity in GCS applications.

458   **4.5 Effect of Sample Heterogeneity**

459   As our samples are taken from drill cores collected at depth at the CarbFix carbon mineralization site, the heterogeneity

460   is larger than in rocks typically used in rock mechanics experiments. The samples investigated in this study exhibit

461   variations in their initial porosity (5-15%, see Table 1), ultimate strength (55-130 MPa) and Young's modulus (12-28

462   GPa). We observed a correlation between the ultimate strength and the elastic modulus of the samples where stiffer

463   samples reach higher peak strengths, consistent with previous reports of an empirical relationship between the

464   unconfined compressive strength and the elastic modulus of sedimentary rocks (see review in Chang et al., 2006). The

465   peak strength however varied inversely with porosity; the dry sample (OR5), which has the highest initial porosity

466   (15%), shows a higher ultimate strength (>105 MPa) and exhibits the lowest creep rate compared to the fluid-saturated

467   experiments where porosity measurements were available (H_2O and H_2O+CO_2 close). Remarkably, the stress

468   sensitivity of the creep strain rate shows consistency ($e^{0.02 - 0.03 \, \sigma}$) in all the fluid saturated experiments (H_2O and

469   H_2O+CO_2 open and close) in spite of these variations in porosity, stiffness and ultimate strength. Moreover, the creep

470   rate at individual stress steps is consistent for experiments with comparable fluid chemistry (H_2O and $H_2O + CO_2$

471 closed) despite a variation in porosity by a factor of 2 in between the samples (Figure 3 and Table 1). These results

472 are a strong argument for the operation of chemical processes that contribute to creep. While variations in porosity

473 resulted in variation in peak strength, they did not seem to affect the absolute creep rates or the sensitivity of creep

474 rate to stress.

475 **5 Conclusions**

476 Through the experimental study of long-term creep deformation of Iceland Basalt, we have demonstrated that:

477 • Transient creep occurred at stress levels significantly below the onset of dilatant cracking.

478 • Presence of an aqueous pore fluid exerted first order control on the creep deformation of the basaltic rocks,
479 while the fluid composition had only a secondary effect under our experimental conditions. At similar
480 differential stress level, the creep rates in fluid-saturated experiments were much higher than the rates in the
481 dry experiment.

482 • A close system tended to favor dissolution over precipitation during carbonation in our experimental setting,
483 whereas precipitation played a more important role in an open system with continuous CO_2 supply.

484 • Larger amount of dilation was observed in fluid saturated experiments than in the dry experiment, as
485 evidenced by both volumetric strain data and micro-structural observations.

486 • Larger low/high amplitude ratios of the AE events and higher AE rates were observed during the phase II
487 creep of the fluid-saturated experiments than the dry experiment, indicating that aqueous fluids promoted
488 stress corrosion processes.

489 • The mechanism governing the creep deformation was brittle, time- and stress-dependent, and could likely be
490 identified as sub-critical dilatant cracking.

491 Overall, our results emphasize the non-negligible role that the creep deformation can potentially play in the long-term

492 deformation of rocks even under low pressure and temperature conditions and calls for more attention to time-

493 dependent processes such as sub-critical micro-cracking in GCS applications. Under our experimental conditions, the

494 creep deformation and the associated fracture development were affected by the presence of aqueous fluids, implying

495 that reactive fluids could potentially alter the fracture patterns and allow mineralization in a greater rock volume during

496 GCS applications. Further detailed studies on the creep deformation under chemically active environment are required

497 to better understand the long-term deformation of rocks in natural systems.

References

Alfredsson, H. A., Hardarson, B. S., Franzson, H. and Gislason, S. R.: CO2 sequestration in basaltic rock at the
Hellisheidi site in SW Iceland: stratigraphy and chemical composition of the rocks at the injection site, Mineral.

511   Mag., 72(1), 1–5, doi:10.1180/minmag.2008.072.1.1, 2008.

512   Alfredsson, H. A., Oelkers, E. H., Hardarsson, B. S., Franzson, H., Gunnlaugsson, E. and Gislason, S. R.: The
513   geology and water chemistry of the Hellisheidi, SW-Iceland carbon storage site, Int. J. Greenh. Gas Control, 12,
514   399–418, doi:10.1016/j.ijggc.2012.11.019, 2013.

515   Anderson, O. L. and Grew, P. C.: Stress corrosion theory of crack propagation with applications to geophysics, Rev.
516   Geophys., doi:10.1029/RG015i001p00077, 1977.

517   Aradóttir, E. S. P., Sonnenthal, E. L., Björnsson, G. and Jónsson, H.: Multidimensional reactive transport modeling
518   of CO2 mineral sequestration in basalts at the Hellisheidi geothermal field, Iceland, Int. J. Greenh. Gas Control, 9,
519   24–40, doi:10.1016/J.IJGGC.2012.02.006, 2012.

520   Atkinson, B. K.: Subcritical crack growth in geological materials, J. Geophys. Res. Solid Earth,
521   doi:10.1029/JB089iB06p04077, 1984.

522   Atkinson, B. K. and Meredith, P. G.: Fracture mechanics of rock- The Theory of Subcritical Crack Growth with
523   Applications to Minerals and Rocks, in Academic Press Geology Series., 1987.

524   Atkinson, G. M., Eaton, D. W. and Igonin, N.: Developments in understanding seismicity triggered by hydraulic
525   fracturing, Nat. Rev. Earth Environ., doi:10.1038/s43017-020-0049-7, 2020.

526   Bakker, E., Hangx, S. J. T., Niemeijer, A. R. and Spiers, C. J.: Frictional behaviour and transport properties of
527   simulated fault gouges derived from a natural CO2 reservoir, Int. J. Greenh. Gas Control, 54, 70–83,
528   doi:10.1016/j.ijggc.2016.08.029, 2016.

529   Baud, P. and Meredith, P. G.: Damage accumulation during triaxial creep of Darley Dale sandstone from pore
530   volumometry and acoustic emission, Int. J. rock Mech. Min. Sci. Geomech. Abstr., doi:10.1016/S1365-
531   1609(97)00060-9, 1997.

532   Baud, P., Zhu, W. and Wong, T.: Failure mode and weakening effect of water on sandstone, J. Geophys. Res. Solid
533   Earth, doi:10.1029/2000jb900087, 2000.

534   Brace, W. F., Paulding, B. W. and Scholz, C. H.: Dilatancy in the fracture of crystalline rocks, J. Geophys. Res.,
535   doi:10.1029/jz071i016p03939, 1966.

536   Brantut, N.: Time-dependent recovery of microcrack damage and seismic wave speeds in deformed limestone, J.
537   Geophys. Res. Solid Earth, 120(12), 8088–8109, doi:10.1002/2015JB012324, 2015.

538   Brantut, N., Baud, P., Heap, M. J. and Meredith, P. G.: Micromechanics of brittle creep in rocks, J. Geophys. Res.
539   Solid Earth, doi:10.1029/2012JB009299, 2012.

540   Brantut, N., Heap, M. J., Meredith, P. G. and Baud, P.: Time-dependent cracking and brittle creep in crustal rocks: A
541   review, J. Struct. Geol., 52(1), 17–43, doi:10.1016/j.jsg.2013.03.007, 2013.

542   Broberg, K. B.: Differences Between Mode I and Mode II Crack Propagation, Pure Appl. Geophys., 163(9), 1867–
543   1879, doi:10.1007/s00024-006-0101-7, 2006.

544   Broecker, W. S.: Climatic change: Are we on the brink of a pronounced global warming?, Science (80-.).,
545   doi:10.1126/science.189.4201.460, 1975.

546   Brzesowsky, R. H., Hangx, S. J. T., Brantut, N. and Spiers, C. J.: Compaction creep of sands due to time-dependent
547   grain failure: Effects of chemical environment, applied stress, and grain size, J. Geophys. Res. Solid Earth, 119(10),
548   7521–7541, doi:10.1002/2014JB011277, 2014.

549   Callow, B., Falcon-Suarez, I., Ahmed, S. and Matter, J. M.: Assessing the carbon sequestration potential of basalt
550   using X-ray micro-CT and rock mechanics, Int. J. Greenh. Gas Control, 70(December 2017), 146–156,
551   doi:10.1016/j.ijggc.2017.12.008, 2018.

552   Chang, C., Zoback, M. D. and Khaksar, A.: Empirical relations between rock strength and physical properties in
553   sedimentary rocks, J. Pet. Sci. Eng., doi:10.1016/j.petrol.2006.01.003, 2006.

554   Charles, R. J. and Hillig, W. B.: The Kinetics of Glass Failure by Stress Corrosion, in Symposium on Mechanical
555   Strength of Glass and Ways of Improving It., 1962.

556 Chester, F. M., Chester, J. S., Kronenberg, A. K. and Hajash, A.: Subcritical creep compaction of quartz sand at
557 diagenetic conditions: Effects of water and grain size, J. Geophys. Res., 112(B6), B06203,
558 doi:10.1029/2006JB004317, 2007.

559 Chester, J. ., Lenz, S. ., Chester, F. . and Lang, R. .: Mechanisms of compaction of quartz sand at diagenetic
560 conditions, Earth Planet. Sci. Lett., 220(3–4), 435–451, doi:10.1016/S0012-821X(04)00054-8, 2004.

561 Dunkel, K. G., Austrheim, H., Renard, F., Cordonnier, B. and Jamtveit, B.: Localized slip controlled by dehydration
562 embrittlement of partly serpentinized dunites, Leka Ophiolite Complex, Norway, Earth Planet. Sci. Lett., 463, 277–
563 285, doi:10.1016/j.epsl.2017.01.047, 2017.

564 Dunning, J. D. and Miller, M. E.: Effects of pore fluid chemistry on stable sliding of Berea sandstone, Pure Appl.
565 Geophys. PAGEOPH, 122(2–4), 447–462, doi:10.1007/BF00874611, 1985.

566 Elkhoury, J. E., Ameli, P. and Detwiler, R. L.: Dissolution and deformation in fractured carbonates caused by flow
567 of CO2-rich brine under reservoir conditions, Int. J. Greenh. Gas Control, 16, S203–S215,
568 doi:10.1016/J.IJGGC.2013.02.023, 2013.

569 Fortin, J., Stanchits, S., Vinciguerra, S. and Guéguen, Y.: Influence of thermal and mechanical cracks on
570 permeability and elastic wave velocities in a basalt from Mt. Etna volcano subjected to elevated pressure,
571 Tectonophysics, 503(1–2), 60–74, doi:10.1016/j.tecto.2010.09.028, 2011.

572 Gadikota, G., Matter, J. M., Kelemen, P. B. and Park, A. H. A.: Chemical and morphological changes during olivine
573 carbonation for CO 2 storage in the presence of NaCl and NaHCO 3, Phys. Chem. Chem. Phys., 16(10), 4679–4693,
574 doi:10.1039/c3cp54903h, 2014.

575 Ghaffari, H. O. and Pec, M.: An ultrasound probe array for a high-pressure, high-temperature solid medium
576 deformation apparatus, Rev. Sci. Instrum., 91(8), 085117, doi:10.1063/5.0004035, 2020.

577 Gislason, S. R. and Hans, P. E.: Meteoric water-basalt interactions. I: A laboratory study, Geochim. Cosmochim.
578 Acta, doi:10.1016/0016-7037(87)90161-X, 1987.

579 Gislason, S. R. and Oelkers, E. H.: Carbon Storage in Basalt, Science (80-.)., 344(6182), 373–374,
580 doi:10.1126/science.1250828, 2014.

581 Gislason, S. R., Wolff-Boenisch, D., Stefansson, A., Oelkers, E. H., Gunnlaugsson, E., Sigurdardottir, H., Sigfusson,
582 B., Broecker, W. S., Matter, J. M. and Stute, M.: Mineral sequestration of carbon dioxide in basalt: A pre-injection
583 overview of the CarbFix project, Int. J. Greenh. Gas Control, 4(3), 537–545, doi:10.1016/j.ijggc.2009.11.013, 2010.

584 Goff, F. and Lackner, K. S.: Carbon dioxide sequestering using ultramafic rocks, Environ. Geosci., 5(3), 89 LP –
585 101, doi:10.1046/j.1526-0984.1998.0a8014.x, 1998.

586 Guglielmi, Y., Cappa, F., Avouac, J. P., Henry, P. and Elsworth, D.: Seismicity triggered by fluid injection-induced
587 aseismic slip, Science (80-.)., doi:10.1126/science.aab0476, 2015.

588 Hangx, S. J. T. and Spiers, C. J.: Reaction of plagioclase feldspars with CO2 under hydrothermal conditions, Chem.
589 Geol., doi:10.1016/j.chemgeo.2008.12.005, 2009.

590 Hansen, L. D., Dipple, G. M., Gordon, T. M. and Kellett, D. A.: CARBONATED SERPENTINITE
591 (LISTWANITE) AT ATLIN, BRITISH COLUMBIA: A GEOLOGICAL ANALOGUE TO CARBON DIOXIDE
592 SEQUESTRATION, Can. Mineral., 43(1), 225–239, doi:10.2113/gscanmin.43.1.225, 2005.

593 Hatton, C. G., Main, I. G. and Meredith, P. G.: A comparison of seismic and structural measurements of scaling
594 exponents during tensile subcritical crack growth, J. Struct. Geol., doi:10.1016/0191-8141(93)90008-X, 1993.

595 Heap, M. J., Baud, P., Meredith, P. G., Bell, A. F. and Main, I. G.: Time-dependent brittle creep in darley dale
596 sandstone, J. Geophys. Res. Solid Earth, 114(7), 1–22, doi:10.1029/2008JB006212, 2009.

597 Heap, M. J., Baud, P., Meredith, P. G., Vinciguerra, S., Bell, A. F. and Main, I. G.: Brittle creep in basalt and its
598 application to time-dependent volcano deformation, Earth Planet. Sci. Lett., 307(1–2), 71–82,
599 doi:10.1016/j.epsl.2011.04.035, 2011.

600 Heard, H. C.: Chapter 7: Transition from Brittle Fracture to Ductile Flow in Solenhofen Limestone as a Function of
601 Temperature, Confining Pressure, and Interstitial Fluid Pressure, Geol. Soc. Am. Mem., doi:10.1130/MEM79-p193,

602   1960.

603   Heilbronner, R. and Barrett, S.: Image Analysis in Earth Sciences, Springer Berlin Heidelberg, Berlin, Heidelberg.,
604   2014.

605   Helmons, R. L. J., Miedema, S. A. and van Rhee, C.: Simulating hydro mechanical effects in rock deformation by
606   combination of the discrete element method and the smoothed particle method, Int. J. Rock Mech. Min. Sci.,
607   doi:10.1016/j.ijrmms.2016.04.018, 2016.

608   Hillig, W. B.: The C-H delayed failure mechanism revisited, Int. J. Fract., doi:10.1007/s10704-006-0025-3, 2006.

609   Iyer, K., Jamtveit, B., Mathiesen, J., Malthe-Sørenssen, A. and Feder, J.: Reaction-assisted hierarchical fracturing
610   during serpentinization, Earth Planet. Sci. Lett., 267(3–4), 503–516, doi:10.1016/j.epsl.2007.11.060, 2008.

611   Jamtveit, B., Putnis, C. V. and Malthe-Sørenssen, A.: Reaction induced fracturing during replacement processes,
612   Contrib. to Mineral. Petrol., 157(1), 127–133, doi:10.1007/s00410-008-0324-y, 2009.

613   Kanakiya, S., Adam, L., Esteban, L., Rowe, M. C. and Shane, P.: Dissolution and secondary mineral precipitation in
614   basalts due to reactions with carbonic acid, J. Geophys. Res. Solid Earth, doi:10.1002/2017JB014019, 2017.

615   Kelemen, P. B. and Hirth, G.: Reaction-driven cracking during retrograde metamorphism: Olivine hydration and
616   carbonation, Earth Planet. Sci. Lett., 345–348, 81–89, doi:10.1016/j.epsl.2012.06.018, 2012.

617   Kelemen, P. B. and Matter, J. M.: In situ carbonation of peridotite for CO_2 storage, Proc. Natl. Acad. Sci. U. S. A.,
618   105(45), 17295–17300, doi:10.1073/pnas.0805794105, 2008.

619   Kelemen, P. B., Savage, H. M. and Hirth, G.: Reaction-Driven Cracking During Mineral Hydration, Carbonation
620   and Oxidation, in Poromechanics V, vol. c, pp. 823–826, American Society of Civil Engineers, Reston, VA., 2013.

621   Kranz, R. L., Harris, W. J. and Carter, N. L.: Static fatigue of granite at 200°C, Geophys. Res. Lett.,
622   doi:10.1029/GL009i001p00001, 1982.

623   Lackner, K. S., Wendt, C. H., Butt, D. P., Joyce, E. L. and Sharp, D. H.: Carbon dioxide disposal in carbonate
624   minerals, Energy, 20(11), 1153–1170, doi:10.1016/0360-5442(95)00071-N, 1995.

625   Lambart, S., Savage, H. M., Robinson, B. G. and Kelemen, P. B.: Experimental Investigation of the Pressure of
626   Crystallization of Ca(OH) 2 : Implications for the Reactive Cracking Process, Geochemistry, Geophys. Geosystems,
627   doi:10.1029/2018GC007609, 2018.

628   Lisabeth, H. P., Zhu, W., Xing, T. and De Andrade, V.: Dissolution-Assisted Pattern Formation During Olivine
629   Carbonation, Geophys. Res. Lett., 44(19), 9622–9631, doi:10.1002/2017GL074393, 2017a.

630   Lisabeth, H. P., Zhu, W., Kelemen, P. B. and Ilgen, A. G.: Experimental evidence for chemo-mechanical coupling
631   during carbon mineralization in ultramafic rocks, Earth Planet. Sci. Lett., 474, 355–367,
632   doi:10.1016/j.epsl.2017.06.045, 2017b.

633   Liteanu, E., Niemeijer, A. R., Spiers, C. J., Peach, C. J. and De Bresser, J. H. P.: The effect of CO_2 on creep of wet
634   calcite aggregates, J. Geophys. Res. Solid Earth, 117(3), doi:10.1029/2011JB008789, 2012.

635   Lockner, D. A.: The role of acoustic emission in the study of rock fracture, Int. J. Rock Mech. Min. Sci.,
636   doi:10.1016/0148-9062(93)90041-B, 1993.

637   Lockner, D. A., Byerlee, J. D., Kuksenko, V., Ponomarev, A. and Sidorin, A.: Observations of Quasistatic Fault
638   Growth from Acoustic Emissions, Int. Geophys., doi:10.1016/S0074-6142(08)62813-2, 1992.

639   Luquot, L. and Gouze, P.: Experimental determination of porosity and permeability changes induced by injection of
640   CO_2 into carbonate rocks, Chem. Geol., 265(1–2), 148–159, doi:10.1016/J.CHEMGEO.2009.03.028, 2009.

641   Macdonald, A. H. and Fyfe, W. S.: Rate of serpentinization in seafloor environments, Tectonophysics, 116(1–2),
642   123–135, doi:10.1016/0040-1951(85)90225-2, 1985.

643   Mani, D., Nirmal Charan, S. and Kumar, B.: Assessment of carbon dioxide sequestration potential of ultramafic
644   rocks in the greenstone belts of southern India, Curr. Sci., 94(1), 53–60, 2008.

645   Matter, J. M. and Kelemen, P. B.: Permanent storage of carbon dioxide in geological reservoirs by mineral
646   carbonation, Nat. Geosci., 2(12), 837–841, doi:10.1038/ngeo683, 2009.

647 Matter, J. M., Takahashi, T. and Goldberg, D. S.: Experimental evaluation of in situ CO2-water-rock reactions
648 during CO2 injection in basaltic rocks: Implications for geological CO2 sequestration, Geochemistry, Geophys.
649 Geosystems, doi:10.1029/2006GC001427, 2007.

650 Matter, J. M., Stute, M., Snaebjornsdottir, S. O., Oelkers, E. H., Gislason, S. R., Aradottir, E. S., Sigfusson, B.,
651 Gunnarsson, I., Sigurdardottir, H., Gunnlaugsson, E., Axelsson, G., Alfredsson, H. A., Wolff-Boenisch, D., Mesfin,
652 K., Taya, D. F. d. l. R., Hall, J., Dideriksen, K. and Broecker, W. S.: Rapid carbon mineralization for permanent
653 disposal of anthropogenic carbon dioxide emissions, Science (80-.)., 352(6291), 1312–1314,
654 doi:10.1126/science.aad8132, 2016.

655 McGrail, B. P., Schaef, H. T., Ho, A. M., Chien, Y. J., Dooley, J. J. and Davidson, C. L.: Potential for carbon
656 dioxide sequestration in flood basalts, J. Geophys. Res. Solid Earth, doi:10.1029/2005JB004169, 2006.

657 McGrail, B. P., Spane, F. A. A., Sullivan, E. C., Bacon, D. H. and Hund, G.: The Wallula basalt sequestration pilot
658 project, Energy Procedia, 4, 5653–5660, doi:10.1016/j.egypro.2011.02.557, 2011.

659 McGrail, B. P., Schaef, H. T., Spane, F. A., Horner, J. A., Owen, A. T., Cliff, J. B., Qafoku, O., Thompson, C. J. and
660 Sullivan, E. C.: Wallula Basalt Pilot Demonstration Project: Post-injection Results and Conclusions, Energy
661 Procedia, 114, 5783–5790, doi:10.1016/j.egypro.2017.03.1716, 2017.

662 Meredith, P. G. and Atkinson, B. K.: Stress corrosion and acoustic emission during tensile crack propagation in
663 Whin Sill dolerite and other basic rocks, Geophys. J. R. Astron. Soc., 75(1), 1–21, doi:10.1111/j.1365-
664 246X.1983.tb01911.x, 1983.

665 Michalske, T. A. and Freiman, S. W.: A Molecular Mechanism for Stress Corrosion in Vitreous Silica, J. Am.
666 Ceram. Soc., doi:10.1111/j.1151-2916.1983.tb15715.x, 1983.

667 Mighani, S., Bernabé, Y., Boulenouar, A., Mok, U. and Evans, B.: Creep Deformation in Vaca Muerta Shale From
668 Nanoindentation to Triaxial Experiments, J. Geophys. Res. Solid Earth, doi:10.1029/2019JB017524, 2019.

669 Nara, Y., Yamanaka, H., Oe, Y. and Kaneko, K.: Influence of temperature and water on subcritical crack growth
670 parameters and long-term strength for igneous rocks, Geophys. J. Int., doi:10.1093/gji/ggs116, 2013.

671 National Academies of Sciences, Engineering, and M.: Negative Emissions Technologies and Reliable
672 Sequestration: A Research Agenda, National Academies Press, Washington, D.C., 2019.

673 Oelkers, E. H., Gislason, S. R. and Matter, J. M.: Mineral carbonation of CO2, Elements, 4(5), 333–337,
674 doi:10.2113/gselements.4.5.333, 2008.

675 Orowan, E.: The fatigue of glass under stress, Nature, 154(3906), 341–343, doi:10.1038/154341a0, 1944.

676 Panozzo, R. É.: Two-dimensional strain from the orientation of lines in a plane, J. Struct. Geol., doi:10.1016/0191-
677 8141(84)90098-1, 1984.

678 Reber, J. E. and Pec, M.: Comparison of brittle- and viscous creep in quartzites: Implications for semi-brittle flow of
679 rocks, J. Struct. Geol., doi:10.1016/j.jsg.2018.05.022, 2018.

680 Reches, Z. and Lockner, D. A.: Nucleation and growth of faults in brittle rocks, J. Geophys. Res. Solid Earth,
681 doi:10.1029/94jb00115, 1994.

682 Renard, F., Gundersen, E., Hellmann, R., Collombet, M. and Le Guen, Y.: Numerical modeling of the effect of
683 carbon dioxide sequestration on the rate of pressure solution creep in limestone: Preliminary results, Oil Gas Sci.
684 Technol., doi:10.2516/ogst:2005023, 2005.

685 Renard, F., Kandula, N., McBeck, J. and Cordonnier, B.: Creep Burst Coincident With Faulting in Marble Observed
686 in 4-D Synchrotron X-Ray Imaging Triaxial Compression Experiments, J. Geophys. Res. Solid Earth,
687 doi:10.1029/2020JB020354, 2020.

688 Rice, J. R.: Thermodynamics of the quasi-static growth of Griffith cracks, J. Mech. Phys. Solids, doi:10.1016/0022-
689 5096(78)90014-5, 1978.

690 Robertson, E. C.: Creep of Solenhofen Limestone Under Moderate Hydrostatic Pressure, pp. 227–244., 1960.

691 Robertson, E. C.: Viscoelasticity of rocks, State Stress Earth's Crust, 181–233, 1964.

692   Rudge, J. F., Kelemen, P. B. and Spiegelman, M.: A simple model of reaction-induced cracking applied to
693   serpentinization and carbonation of peridotite, Earth Planet. Sci. Lett., 291(1–4), 215–227,
694   doi:10.1016/j.epsl.2010.01.016, 2010.

695   Rutter, E. H.: The influence of interstitial water on the rheological behaviour of calcite rocks, Tectonophysics,
696   doi:10.1016/0040-1951(72)90003-0, 1972.

697   Rutter, E. H. and Hackston, A.: On the effective stress law for rock-on-rock frictional sliding, and fault slip triggered
698   by means of fluid injection, Philos. Trans. R. Soc. A Math. Phys. Eng. Sci., 375(2103), doi:10.1098/rsta.2016.0001,
699   2017.

700   Scholz, C. H.: Mechanism of creep in brittle rock, J. Geophys. Res., doi:10.1029/JB073i010p03295, 1968.

701   Scholz, C. H.: Static fatigue of quartz, J. Geophys. Res., doi:10.1029/JB077i011p02104, 1972.

702   Seifritz, W.: CO2 disposal by means of silicates, Nature, 345(6275), 486–486, doi:10.1038/345486b0, 1990.

703   Skarbek, R. M., Savage, H. M., Kelemen, P. B. and Yancopoulos, D.: Competition Between Crystallization-Induced
704   Expansion and Creep Compaction During Gypsum Formation, and Implications for Serpentinization, J. Geophys.
705   Res. Solid Earth, 123(7), 5372–5393, doi:10.1029/2017JB015369, 2018.

706   Snæbjörnsdóttir, S. Ó. and Gislason, S. R.: CO2 Storage Potential of Basaltic Rocks Offshore Iceland, Energy
707   Procedia, 86, 371–380, doi:10.1016/j.egypro.2016.01.038, 2016.

708   Snæbjörnsdóttir, S. Ó., Gislason, S. R., Galeczka, I. M. and Oelkers, E. H.: Reaction path modelling of in-situ
709   mineralisation of CO2 at the CarbFix site at Hellisheidi, SW-Iceland, Geochim. Cosmochim. Acta, 220, 348–366,
710   doi:10.1016/j.gca.2017.09.053, 2018.

711   Snæbjörnsdóttir, S. Ó., Sigfússon, B., Marieni, C., Goldberg, D., Gislason, S. R. and Oelkers, E. H.: Carbon dioxide
712   storage through mineral carbonation, Nat. Rev. Earth Environ., doi:10.1038/s43017-019-0011-8, 2020.

713   Terzaghi, K.: Theoretical soil mechanics, Chapman And Hall, Limited., London., 1943.

714   Vajdova, V., Baud, P., Wu, L. and Wong, T. fong: Micromechanics of inelastic compaction in two allochemical
715   limestones, J. Struct. Geol., doi:10.1016/j.jsg.2012.07.006, 2012.

716   Wong, L. N. Y. and Einstein, H. H.: Systematic evaluation of cracking behavior in specimens containing single
717   flaws under uniaxial compression, Int. J. Rock Mech. Min. Sci., doi:10.1016/j.ijrmms.2008.03.006, 2009.

718   Xing, T., Zhu, W., Fusseis, F. and Lisabeth, H. P.: Generating porosity during olivine carbonation via dissolution
719   channels and expansion cracks, Solid Earth, 9(4), 879–896, doi:10.5194/se-9-879-2018, 2018.

720   Zakharova, N. V., Goldberg, D. S., Sullivan, E. C., Herron, M. M. and Grau, J. A.: Petrophysical and geochemical
721   properties of Columbia River flood basalt: Implications for carbon sequestration, Geochemistry, Geophys.
722   Geosystems, 13(11), 1–22, doi:10.1029/2012GC004305, 2012.

723   Zhang, X. and Spiers, C. J.: Compaction of granular calcite by pressure solution at room temperature and effects of
724   pore fluid chemistry, Int. J. Rock Mech. Min. Sci., doi:10.1016/j.ijrmms.2005.05.017, 2005.

725   Zhang, X., Spiers, C. J. and Peach, C. J.: Compaction creep of wet granular calcite by pressure solution at 28°C to
726   150°C, J. Geophys. Res. Solid Earth, doi:10.1029/2008JB005853, 2010.

727   Zhang, X., Spiers, C. J. and Peach, C. J.: Effects of pore fluid flow and chemistry on compaction creep of calcite by
728   pressure solution at 150°C, Geofluids, 11(1), 108–122, doi:10.1111/j.1468-8123.2010.00323.x, 2011.

729   Zhang, Z. L., Xu, W. Y., Wang, W. and Wang, R. B.: Triaxial creep tests of rock from the compressive zone of dam
730   foundation in Xiangjiaba Hydropower Station, Int. J. Rock Mech. Min. Sci., doi:10.1016/j.ijrmms.2012.01.003,
731   2012.

732   Zhu, W. and Wong, T.: The transition from brittle faulting to cataclastic flow: Permeability evolution, J. Geophys.
733   Res. Solid Earth, doi:10.1029/96jb03282, 1997.

734   Zhu, W., Baud, P. and Wong, T. F.: Micromechanics of cataclastic pore collapse in limestone, J. Geophys. Res.
735   Solid Earth, doi:10.1029/2009JB006610, 2010.

736   Zhu, W., Fusseis, F., Lisabeth, H. P., Xing, T., Xiao, X., De Andrade, V. and Karato, S.: Experimental evidence of
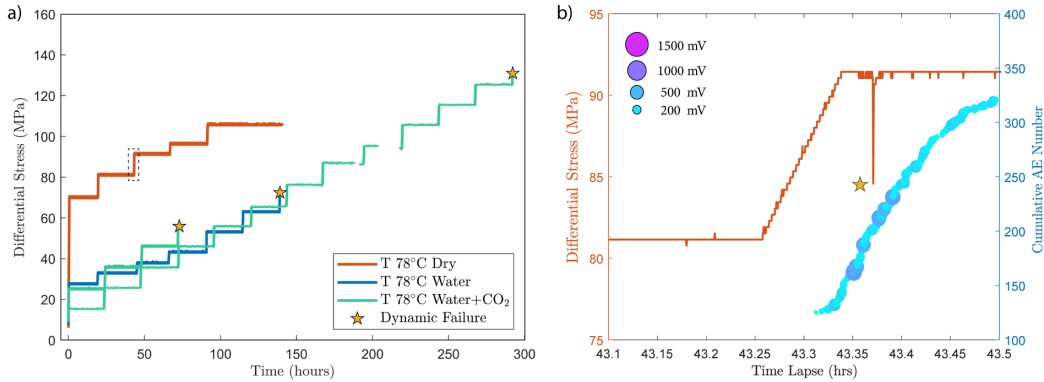
737   reaction-induced fracturing during olivine carbonation, Geophys. Res. Lett., 43(18), 9535–9543,
738   doi:10.1002/2016GL070834, 2016.
739

Appendices

A.1 Experimental Procedures


Figure A1 a) Differential stress vs time plot of experiments conducted at temperature of 78°C. The dry experiment (red) was ceased before dynamic failure occurred in the sample. b) A temporary stress drop was observed (highlighted by the dashed rectangle in a)) during the primary creep of the dry experiment at creep stress of ~90 MPa accompanied by the occurrence of high amplitude AEs.

A.2 Phase I to Phase II Transient Creep Transition

Selection of the phase II transient creep from the mechanical data is based on the calculated strain rate using first derivative of the strain curve vs. time at different stress levels (Figure A2). The plot of strain rate vs strain further supported that the strain rate evolution slows down during the identified phase II creep.
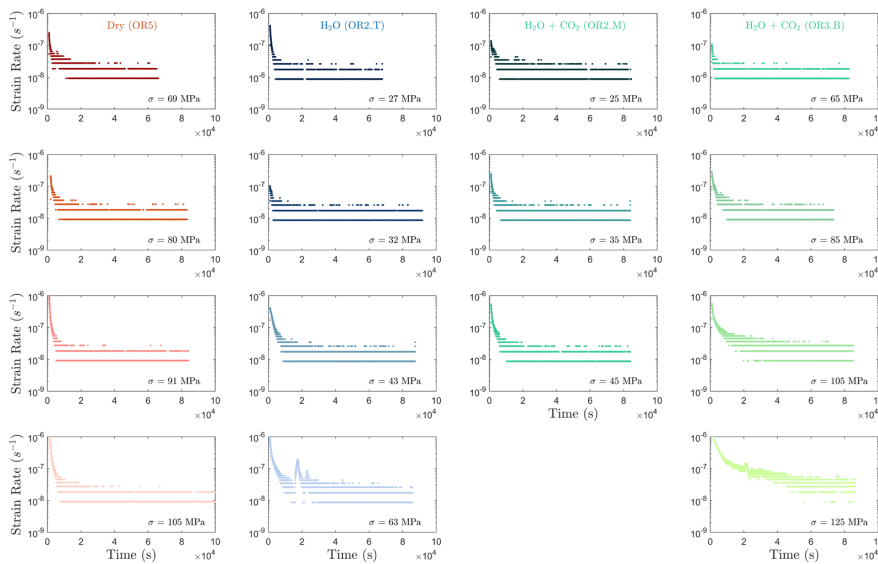
752 **Figure A2** Strain rate evolution calculated from the first derivative of the strain vs. time data. It can be observed that
753 the strain rates generally become constant 10,000 s (≈2.8 h) after the load stepping in most steps.
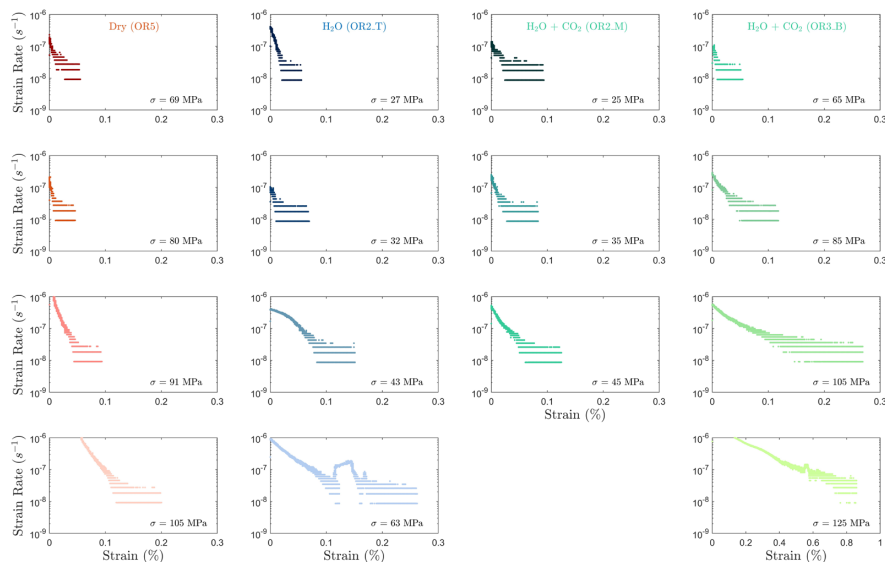

754

755 **Figure A3** Plot of strain rate evolution vs. strain.

756 To consistently analyze the transition between phase I and phase II of the transient creep, we fit the evolution of phase
757 I creep strain over time using a power-law function and the phase II creep strain as a linear function (Figure A3 a).
758 The measured strain data point that is the closest to the intersection of the two fitting functions is selected as the
759 inflection point, i.e., the transition from phase I to phase II transient creep deformation. Figure A3 b and c shows the
760 logarithmic and power-law fitting methods used for the time evolution of creep strain (ε). With the 24 hrs observation
761 window of our experiment.
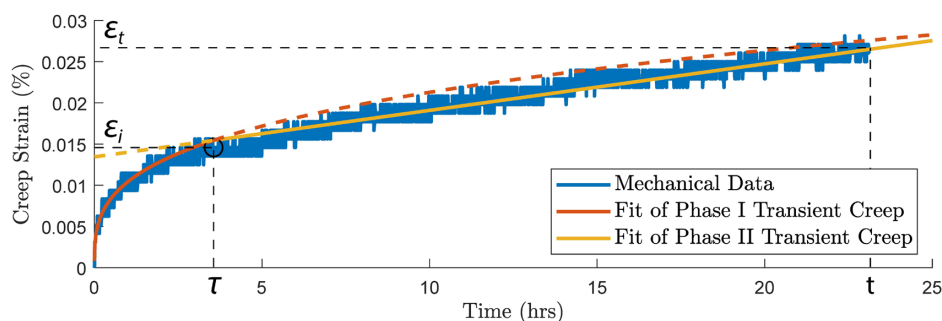
762

763 **Figure A4** illustration of the method used to pick up the transition (circle) from phase I to phase II transient creep
764 deformation. a) Two phase model for the time evolution of creep strain. The transition (circle) from phase I to phase
765 II creep deformation is selected based on the intersection of the power-law fit function of phase I creep (red) and linear
766 fit function of the phase II creep (yellow).

A.3 Creep Strain/Stress Models

The strain rate during phase II creep deformation is generally described using the power law form (e.g. Atkinson, 1984; Meredith and Atkinson, 1983):

$$d\varepsilon/dt = A\sigma^n \qquad \text{(Eq. A1)}$$

or the exponential form (e.g. Charles and Hillig, 1962):

$$d\varepsilon/dt = Be^{\eta\sigma} \qquad \text{(Eq. A2)}$$

where ε is the creep strain and σ is the differential stress. A, B, n and η are constants. Both models have described our laboratory data well. The exponential model seems to be slightly better than the power law model when comparing the R^2 factors.
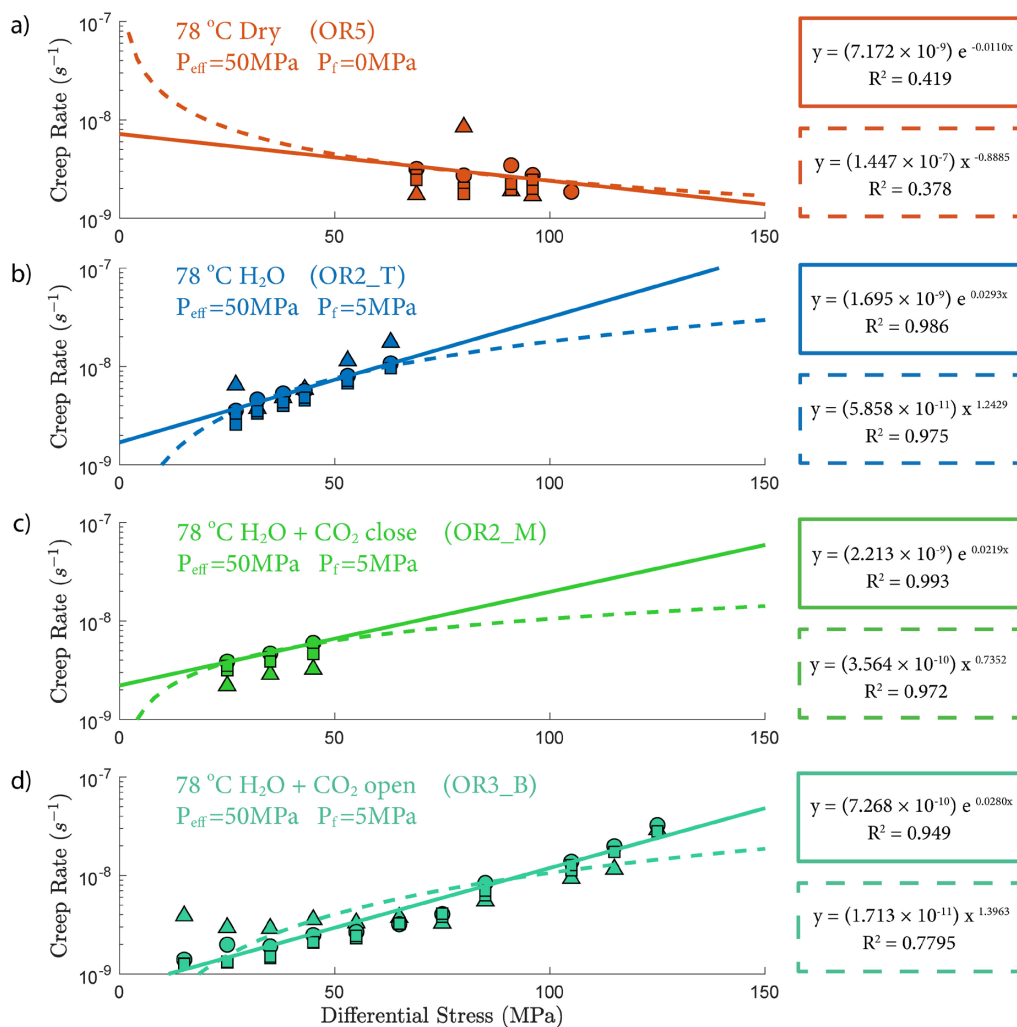

Figure A5 Power-law (dash line) and exponential (solid line) fit of creep rate/stress relationship. The strain rates are calculated from strain measurement from main ram displacement (circle), strain gauge (triangle) and LVDTs (square).
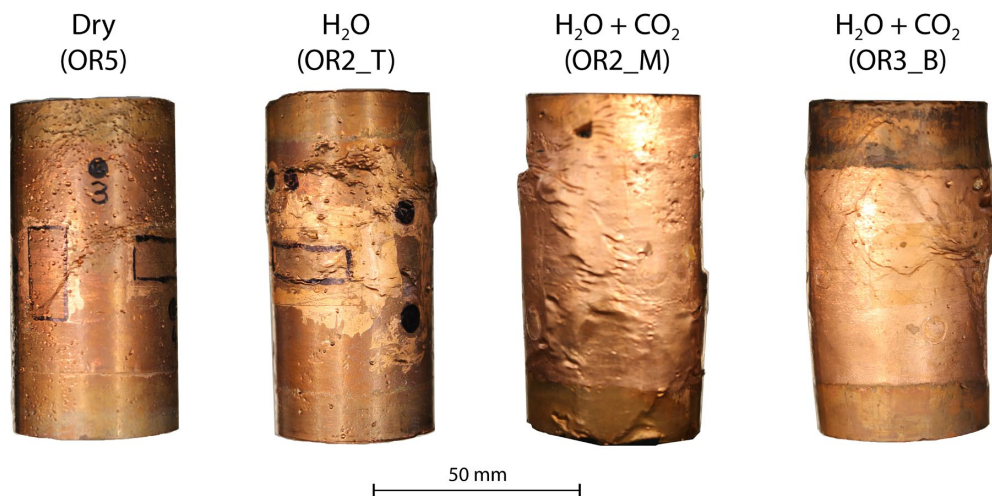
Solid Earth
Discussions

779 **A.4 Gutenberg-Richter b-value**

780 Figure A6 shows the fitting of the Gutenberg-Richter b-value from different experiments at various stress levels.
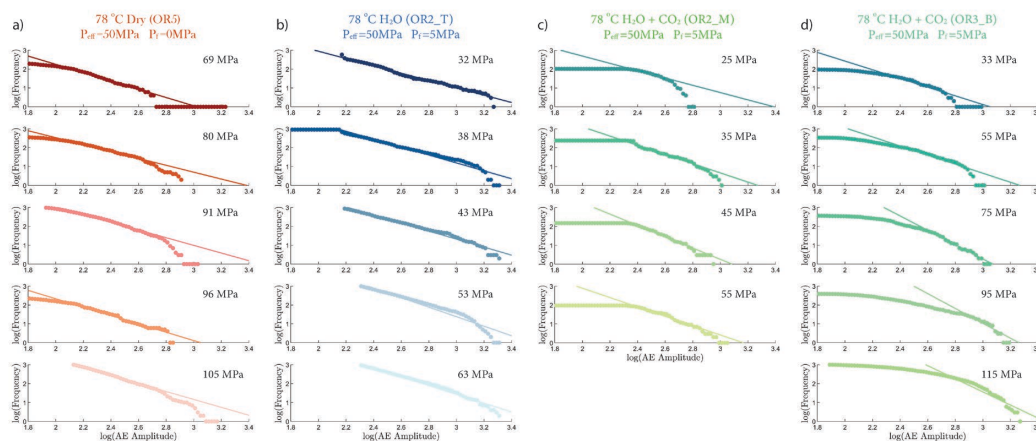
781
782 **Figure A6** Statistics of AE amplitudes for Gutenberg-Richter b-value calculation from a) dry, b) H_2O c) H_2O+CO_2
783 close and d) H_2O+CO_2 open experiments.

784 **A.5 Samples after Deformation**

785
786 **Figure A7** Photo of samples after deformation. The dry sample did not reach the final dynamic failure before
787 experiment was halted.

788 **A.6 Elastic Modulus**

789 The Young's modulus (E) of the sample is calculated based on the strain measurement during the elastic loading,
790 using the following equation:

791
$$E = \frac{\Delta\sigma}{\Delta d/L}$$
(Eq. A4)

792 where $\Delta\sigma$ is the differential stress, d is the displacement of main ram piston and L is the length of the sample.
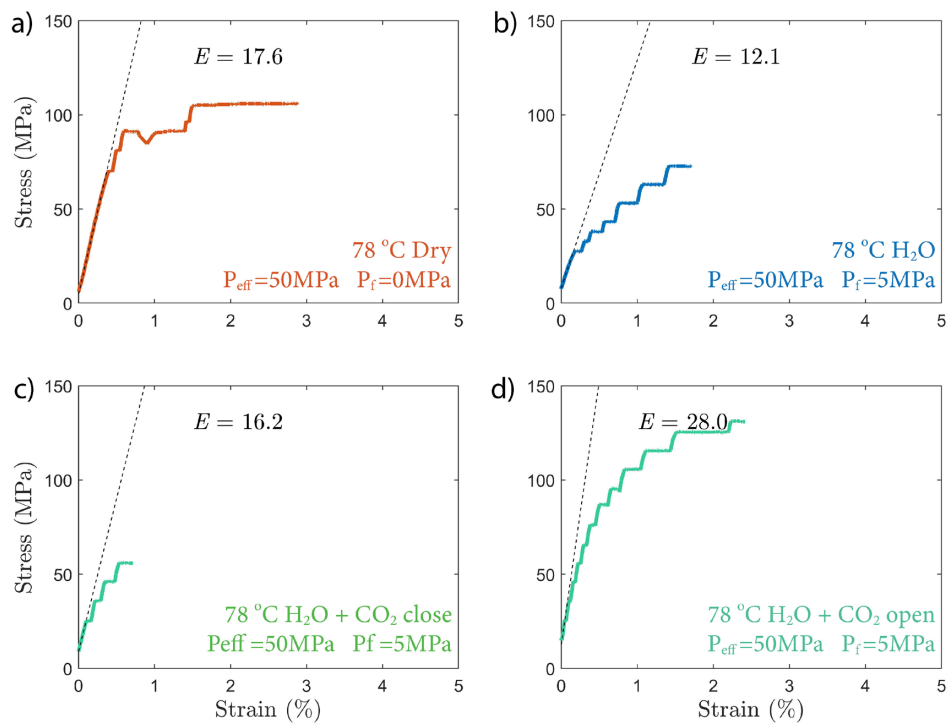
Figure A8 Elastic modulus calculated from strain vs stress plots from a) dry, b) H_2O c) H_2O+CO_2 close and d) H_2O+CO_2 open experiments.